

Stellar Orbits Near Sagittarius A*

A. Eckart

I.Physikalisches Institut, Universität zu Köln, Zùlpicher Str.77, 50937 Köln, Germany

and

R. Genzel, T. Ott, R. Schödel

Max-Planck-Institut für extraterrestrische Physik (MPE), D-85740 Garching, Germany

Received _____; accepted _____

ABSTRACT

The SHARP/NTT stellar proper motion data now cover an interval from 1992 to 2000 and allow us to determine orbital accelerations for some of the most central stars. We confirm the stellar acceleration measurements obtained by Ghez et al. (2000) with NIRC at the Keck telescope. Our analysis differs in 3 main points from that of Ghez et al.: 1) We combine the high precision but shorter time scale NIRC/Keck data with the lower precision but longer time scale SHARP/NTT data set; 2) We statistically correct the observed accelerations for geometrical projection effects; 3) We exclude star S8 from the analysis of the amount and position of the central mass.

From the combined SHARP/NTT and NIRC/Keck data sets we show that the stars S2, and most likely S1 and S8 as well, are on bound, fairly inclined ($60^\circ < i < 80^\circ$), and eccentric ($0.4 < e < 0.95$) orbits around a central dark mass. The combination of both data sets results in a position of this central mass of $48_{-24}^{+54} \text{ mas}$ E and $18_{-61}^{+42} \text{ mas}$ S of the nominal radio position of Sgr A*. The mean statistically corrected enclosed mass derived from accelerations is $M_{acc} = (5 \pm 3) \times 10^6 M_\odot$ with current radial separations of S1 and S2 from SgrA* of about $8 - 10 \text{ mpc}$. This enclosed mass estimate is derived from *individual* stellar orbits as close to the massive black hole at the center of the Milky Way as currently possible. Although the uncertainties are large this estimate is fully consistent with the enclosed mass range of $(2.6 - 3.3) \times 10^6 M_\odot$ derived by Genzel et al. (2000) from radial and/or proper motion velocities of a homogenized sample of sources.

Star S8 was excluded from the analysis, since for the current proper motion velocity and radial separation from the center we find that the measured acceleration requires orbital motion around a compact object with a mass in excess of $3 \times 10^6 M_\odot$. The data suggest that this star *either* was or is subject to a close interaction with a different object *or* that its position measurements are influenced by the emission of a different cluster star. Therefore, we base the analysis of the enclosed mass solely on the available data for S1 and S2. We also discuss two late type stars with projected separations from SgrA* of about $0.5''$ and $1''$. In addition to proper motions these stars have known radial velocities. Orbit calculations indicate that those stars are very likely at larger physical distances from the center and part of the larger scale central stellar cluster with a core radius of approximately 0.3 pc .

Subject headings: BLACK HOLE PHYSICS, ASTROMETRY, CELESTIAL MECHANICS, STELLAR DYNAMICS, GALAXY: CENTER, INFRARED: GENERAL

1. INTRODUCTION

High resolution near-infrared imaging and spectroscopy with large telescopes resulted in a determination of the amount and concentration of mass at the center of the Milky Way (Sellgren et al. 1990, Krabbe et al., 1995, Haller et al. 1996, Eckart & Genzel 1996, Genzel et al. 1998, Ghez et al. 1998, Genzel et al. 2000). Diffraction limited images, proper motions and most recently the detection of acceleration of stars in the vicinity of the compact radio source Sgr A* (Ghez et al. 2000, Eckart et al. 2000a) have led to the conclusion that this source is associated with a central black hole with a mass of about $3 \times 10^6 M_{\odot}$. Using the MPE speckle camera SHARP at the 3.5 m New Technology Telescope (NTT) of the European Southern Observatory (ESO) from 1992 to 2000 we have been conducting a program to study the properties of the central nuclear stellar cluster via near-infrared high spatial resolution measurements. This program has resulted in the very first detection of proper motions of stars that correspond to velocities of up to 1400 km/s in the central arcsecond in the vicinity of Sgr A* (Eckart & Genzel 1996, 1997). These results had been confirmed by Ghez et al. (1998) using NIRC on the Keck telescope. On the 1.6σ to 3σ level we have now detected orbital curvatures of the stars S1, S2, and S8 which confirm the recent results by Ghez et al. (2000).

Over the past 8 years the observed motions translate into a two dimensional velocity dispersion of the stars in the central arcsecond (corrected for the measurement error) of the order of 600 km/s. Overall the stellar motions do not deviate strongly from isotropy and are consistent with a spherical isothermal stellar cluster (Genzel et al. 2000). However, a small deviation from isotropy is found for the sky-projected velocity components of the young, early type stars. Most of the bright HeI emission line stars are on tangential orbits. This overall rotation could be a remnant of the original angular momentum pattern in the interstellar cloud from which these stars were formed. The projected radial and tangential proper motions of the fainter, fast moving stars within $\approx 1''$ from SgrA* (the ‘SgrA* cluster’) suggest that they may largely be moving on very eccentric orbits. Speckle spectroscopy with SHARP at the NTT (Genzel et al. 1997) and slit spectroscopy with ISAAC at the VLT (Eckart, Ott, Genzel 1999, Figer et al. 2000) suggest that several of them are early type stars. This is consistent with the idea that these stars are members of the early type cluster with small angular momentum and therefore fell into the immediate vicinity of SgrA* (Genzel et al. 2000, Gerhard 2000, see also discussion in Ghez et al. 2000).

The detection of orbital curvature for 3 central stars now allows us for the first time to constrain their orbital elements and to investigate the central mass distribution at the smallest currently accessible separations from Sgr A*. In the following subsection 1.1 we give a summary of why it is worthwhile to determine stellar orbits near the dark mass at the Galactic Center and give a general description of how that can be done best. In section 2 we present the new proper motion and acceleration data and derive the position of the central dark mass. In section 3 we show how the acceleration measurements can be used to obtain an enclosed mass estimate. In section 4 we then make use of the enclosed mass and its position and discuss possible orbital solutions for several of the central stars. Finally a

summary and conclusions are given in section 5.

1.1. Stellar orbits and the central mass distribution

The point source sensitivities currently reached in near infrared observations of the central stellar cluster are of the order of $K \sim 16 - 17$ at an angular resolution of 50 - 150 mas (Eckart & Genzel 1996, Ghez et al. 1998, Genzel et al. 2000, Ghez et al. 2000). These current limits are mainly a result of the imaging techniques at the diffraction limit and not due to the sensitivity of the instrumentation. With these values the analysis of the central mass distribution for separations of less than $0.5''$ (~ 20 mpc) from the radio point source SgrA* has to be based on detailed measurements of individual stellar orbits. We assume that the trajectories of stars can be approximated by Keplerian shaped orbits around a central mass.

Relative Keplerian orbits are described by 6 orbital elements: three angles, the eccentricity e , the semi-major axis a and a reference time T for a defined position (i.e. the periastron). Currently for a few of the early type high velocity S-sources as well as two late type stars that are close to the center in projection, our detailed orbital analysis (section 4) can only be based on 5 known quantities that constrain the orbits. In addition to the projected positions and proper motions these are the orbital curvatures (for the S-sources) and the line of sight velocities (for the late type stars). However, for visual binaries - as is the case for a combination of the mass at the center of the Galaxy and any of the fast moving stars in its vicinity - all these orbital elements can be derived from a sufficiently large section of the orbit, except for the sign of the inclination. This has to be inferred from Doppler shifts via spectroscopy. The visual binaries situation holds if the exact position of the black hole on the near-infrared images is known (see Menten et al. 1996). The orbital period and central mass can then be determined via Kepler's third law and the equation of motion i.e. from Newton's law. Here we present a first step to reach that goal using the combined SHARP/NTT and NIRC/Keck data sets.

The orbital analysis in the presence of a possibly partially extended central mass has to await the detection of fainter stars ($K \geq 17$) closer (< 2 mpc) to SgrA* or the availability of long period measurements (of the order of 100 years or more; see section 4.2) of the presently known high velocity stars within the central arcsecond. The expected orbits have been discussed in the context of the Galactic Center by Rubilar & Eckart (2001, see also Fragile & Mathews, 2000, Munyaneza, Tsiklauri & Viollier, 1998, and Jaroszyński, 1998). The shortest orbital time scales that could be observed in the near future will be of the order of only a few months. These measurements are well within reach using the new instrumentation (VLT, Keck and LBT interferometers; see Rubilar & Eckart 2001, Eckart, Ott, Genzel 2001a, 2001b).

2. ACCELERATIONS

From stellar orbital accelerations we can determine the position of the central mass. They can also be used to derive an additional estimate of the enclosed mass, help to constrain the stellar orbital parameters, and to show whether or not the high velocity stars in the vicinity of SgrA* are bound. In the following we first present the results from the SHARP/NTT data and then describe how we determine the position of the dark mass from the combined SHARP/NTT and NIRC/Keck data sets.

2.1. Stellar accelerations and proper motions

In order to derive accelerations a precise measurement of the change in proper motion velocities is required. Such a measurement can only be performed for stars that are bright, well separable from each other, and close enough to the center in order to show detectable accelerations. At the Galactic center the stars S1, S2, and S8 fulfill this requirement and a curvature of their trajectories has already been detected by Ghez et al. (2000). In order to estimate stellar accelerations from the SHARP/NTT data we have used three different methods: a) variation of proper motion velocities as a function of time, b) parabolic fits to the time position plots and c) fitting Keplerian orbits to the observed data. The results of all three methods are in good agreement and give for stars S1, S2, and S8 accelerations similar to those reported by Ghez et al. (2000). In the following we discuss properties and results of the three methods in more detail.

We prefer to estimate the stellar accelerations via the *variation of proper motion velocities* since this method stays closest to the data. The only requirement is that over a period of 3 to 4 years a linear fit to the data results in reliable estimates of proper motions. The SHARP/NTT proper motion data set covers the time interval from 1992 till 2000 and allows us to derive and confirm for the stars S1, S2, and S8 curvatures of their orbits on the 1.6σ to 3σ level. In Fig. 1 (see also Tab. 1) we show the offset positions from SgrA* in declination and right ascension as a function of time. In the case of S1, S2, and S8 we compare them to parabolic functions (see below). Linear fits to the first and second half of the data sets for these three stars are shown by Eckart, Ott, Genzel (2001a, 2001b) and clearly result in different slopes over successive time intervals. This difference in slopes divided by the time difference between the two intervals is a direct measure of the orbital curvature. We divided the data into an early (1992 - 1996) and a late epoch (1997 - 2000). For each epoch we calculated three velocities from data in different sub-intervals. Individual accelerations were then estimated from quotients of all combinations of velocity and time differences between the early and late epoch. We verified the method by comparing the results to those obtained by the other two methods. We also applied it to the data shown in Fig.2 in Ghez et al. (2000) and reproduced the acceleration values quoted in their Table.1

for the time averaged epoch ¹ 1997.6. In Tab. 1 we compare the total accelerations and their 1σ uncertainties for the three stars S1, S2, and S8 as derived from the SHARP/NTT and the NIRC/Keck data. The data agree to within less than 3.3σ .

A *parabolic fit* is adequate as long as the acceleration is nearly constant over the observed orbit segment. This approximation is not always justified for the entire 8 years of SHARP/NTT observations analyzed here. In particular, star S2 may have completed about half of its orbit during this period. Depending on the observed orbital section a parabolic fit may therefore result in an inaccurate estimate of the acceleration. We have, however, used this method for the purpose of comparison. In Fig.1 we show the data together with parabolic functions that have curvatures as listed in Tab.1. For stars S1, S2 parabolic fits give similar results. For S8 parabolic fits indicate a curvature closer to 2.3mas yr^{-2} (as plotted in Fig.1) rather than 3.3mas yr^{-2} which is, however, well within the errors of the value derived above.

Fitting Keplerian orbits to the data has the advantage that it provides the appropriate dependence of the projected positions as a function of time. It has the disadvantage that it assumes the presence of Keplerian orbits and therefore requires knowledge of the enclosed mass and mass density. In section 4 we show that the enclosed mass and mass density estimates derived from accelerations are in agreement with a compact $3 \times 10^6 M_\odot$ central object. In section 4 we make use of this fact and fit Keplerian orbits to the data. For the stars S1 and S2 the range of Keplerian accelerations is in close agreement with our estimates from the other two methods. For S8 the observed acceleration lies well above the prediction from Keplerian orbits. Reasons for that are discussed in detail in section 4.2.2.

Determination of Proper motions: In the presence of significant orbital curvature a precise knowledge of positions and proper motion velocities for a given reference epoch is required in order to carry out orbit calculations. As reference epochs we chose the centers of the time intervals covered by the SHARP/NTT and NIRC/Keck data sets. In Tab. 2 we list the positions that we derived for those epochs from our own data and the data presented by Ghez et al. (2000). In both cases the near-infrared positions are measured relative to the radio position of SgrA* (Menten et al. 1996). For S1 and S2 the accelerations given in Tab. 1 correspond to a yearly change of the proper motion velocity of about 80-160 km/s. This is of the order of both the mean measurement uncertainty and the mean differences in proper motion velocities between the SHARP/NTT and NIRC/Keck data sets (with a time difference of about 1 year between central epochs; Eckart & Genzel 1996, Ghez et al. 1998, Genzel et al. 2000, Ghez et al. 2000). In order to combine the SHARP/NTT and NIRC/Keck data sets and to obtain higher precision proper motion values for orbital

¹ Our assessment is that the acceleration values quoted in Table.1 by Ghez et al. (2000) must correspond to the time averaged epoch 1997.6 rather the epoch 1995.53 as mentioned in the corresponding figure caption. Combining the high proper motions of S1 and S2 with the 1995.53 positions - these accelerations would otherwise result in a position of the central mass approximately 0.15" further north compared to what is shown in their Fig.3

calculations we have used our acceleration values and the proper motion velocities for epoch 1995.4 by Ghez et al. (1998) to derive mean proper motion velocities for the two reference epochs 1996.5 for the SHARP/NTT data set and 1997.6 for the NIRC/Keck data set (listed in Tab. 3; see also tables in the Appendix).

We have also investigated the proper motion data of other stars within the SgrA* cluster. The number of further candidates that would allow us to detect curvature from the present SHARP/NTT data set is small. Star S3 apparently became fainter and disappeared - stars S4, S5, and S6 are in a crowded area with S4 even being multiple - and S9 is too faint and is approaching S10 (see notes in appendix of Genzel et al. 1997). In addition to S1, S2, and S8 the best candidates for detecting orbital curvature, in terms of their brightness and source crowding, are S7, S10, S11. In Fig. 1 we show the proper position time diagrams for these three stars and list their separations from Sgr A* and upper limits for their accelerations in Tab. 1.

In addition to the central early type stars there are two late type stars with projected separations of only about 0.5" and 1" listed in Tab.1 as S18 and star No.25, respectively. Those stars are discussed in detail in section 4. In Fig. 2 we show the proper position time diagrams for these two stars that show no significant curvature.

2.2. The Position of the central mass

The accelerations are consistent with recent results by Ghez et al.(2000) and imply that the three stars orbit a central, compact mass. For each of the two sources S1 and S2 the acceleration values define an acceleration vector at an angle ϕ that should point towards the central source. Here we assume that the probability for the location of the central mass is uniform in ϕ . In Fig. 3 the stars S1 and S2 have been plotted at their time averaged position resulting from the corresponding data sets. The measurement uncertainties define an error cone. For the presentation in Fig. 3 the dashed and dotted lines indicate an error cone that corresponds to a width of 2σ in deviation from the nominal direction indicated by the acceleration vector. In order to determine the location of the central mass we perform a maximum likelihood (ML) analysis. As a ML score we use

$$\log(ML) = -\chi_{S1}^2/2 - \chi_{S2}^2/2 \quad . \quad (1)$$

The thin contour lines in Fig. 3 indicate the locations at which $\log(ML)$ drops by 0.5 below the corresponding peak values. Here $\chi^2 = (\phi - \phi_0)^2/(\Delta\phi)^2$, ϕ_0 denotes the angle of the acceleration vector, ϕ the angle of any radial line within an error cone, and $\Delta\phi = \sigma$ the half width of the cone. The central filled circle in Fig. 3 marks the radio position of SgrA* and corresponding uncertainties of ± 30 mas. Using the observed curvature value and the enclosed mass range of 2.6 to $3.3 \times 10^6 M_\odot$ imposes a limit on the projected distance of S1 and S2 from SgrA*. For the SHARP/NTT data this leads to an improvement in the

determination of the SgrA* position. We account for this effect in Fig. 3 by multiplying the $\log(ML)$ scores of the error cones with a Gaussian prior of the appropriate $1/e$ width centered on the time averaged positions of S1 and S2. From the projection of the 1σ contour line (thin contour line E of the center in Fig. 3) the multiplied probabilities derived from the SHARP/NTT and NIRC/Keck data result in a position of a central dark mass of $48_{-24}^{+54} mas$ E and $18_{-61}^{+42} mas$ S of the nominal radio position of Sgr A*. Within these limits the central mass is located at the 68.5% confidence level ($\Delta\chi = 1.0$). At the 90% confidence level ($\Delta\chi = 2.71$) the central mass is located in an interval given by $48_{-48}^{+109} mas$ E and $18_{-133}^{+72} mas$ S (thick contour line E of the center in Fig. 3). Fig. 3 shows that at the current $\pm 30 mas$ uncertainty of the radio position of Sgr A* the presently available accelerations of stars S1 and S2 alone are fully consistent with the hypothesis that the radio source SgrA* is coincident with the center of the dark mass.

3. THE ENCLOSED MASS

Assuming Keplerian orbits the observed projected stellar accelerations allow us only to derive lower limits to the enclosed mass. By inferring an estimate of the true physical separation of the stars from the center these lower limits can be statistically corrected for projection effects and compared to previous estimates of the amount and compactness of the enclosed dark mass. In section 3.1 we first determine the volume that contains the three stars S1, S2, and S8, describe in section 3.2.1 how we use this information to correct for projection effects, verify the validity of that method in section 3.2.2, and then apply it in section 3.2.3 to the observed data.

3.1. Location of stars relative to Sgr A*

In Fig. 4 we plot the quantities that are relevant in describing the position of stars relative to the center of the Galaxy. The line of sight position of individual stars with respect to the plane of the sky containing Sgr A* is unknown. A correction for a geometrical projection of the acceleration values can, however, be carried out statistically by simply estimating the volume that contains the central stars S1, S2, and S8. In order to derive an estimate of this volume we may use the proper motion velocities and projected positions of these stars in comparison to the velocity dispersions and number density as a function of the true (non projected; 3-dimensional) radius r . The central fast moving stars have significantly curved orbits. It is therefore unlikely that these fast moving stars are objects on highly elliptical orbits ($e > 1$) that just happen to fly by the central position on almost linear trajectories. In the following we argue that the sources S1, S2, and S8 are likely located within a spherical volume of radius $15 \pm 3 mpc$ ($0.4'' \pm 0.1''$).

Estimate from velocities and positions: In the following R denotes the projection of the 3-dimensional separation r of the star from the center and V_{star} the projection

of the 3-dimensional velocity v_{star} of the star. An estimate of the size can be obtained by comparing the proper motion velocities V_{star} to the 3-dimensional velocity dispersion obtained from the parameterized functional form of the true number density distribution $n(r)$ and the true radial and tangential velocity dispersions $\sigma_r(r)$ and $\sigma_t(r)$ of the best anisotropic Jeans model (Genzel et al. 2000). Those quantities are integrated along the line of sight at the projected separation R from Sgr A* of the individual stars (formulae 5 and 6 in Genzel et al. 2000). This way we use the projected position and velocity information for each of the stars simultaneously. Both V_{star} and R_{star} are lower limits to v_{star} and r_{star} . For the probability of a star to exhibit a proper motion velocity V in excess of V_{star} we can therefore write

$$P(V > V_{star}, R) \geq P(V > V_{star}, r) \geq P(V > v_{star}, r) \quad . \quad (2)$$

For a given velocity dispersion $\sigma^2(r) = \sigma_r^2(r) + 2\sigma_t^2(r)$ the probability $P(V > V_{star}, r)$ can be calculated via

$$P(V > V_{star}, r) = 1 - P(V \leq V_{star}, r) = 1 - \int_0^{V_{star}} \frac{1}{\sigma^2(r)} v \exp(-v^2/(2\sigma^2(r))) dv \quad . \quad (3)$$

The velocity dispersion $\sigma(r)$ and therefore also the probability $P(V > V_{star}, r)$ decrease with increasing radii r . For fast stars it becomes increasingly unlikely that they belong to statistical samples at correspondingly larger radii. Therefore, we interpret $P(V > V_{star}, r)$ as a measure of how likely it is that the star belongs to a sample of stars at that radius r or larger. Using R instead of r we can calculate $P(V > V_{star}, R)$ as an upper limit of this probability $P(V > V_{star}, r)$. The mean probability of the three stars S1, S2, and S8 to belong to samples of stars at the corresponding radii R_{S1} , R_{S2} , and R_{S8} - or larger - is only about $P_{init} = 33\%$. This implies that the mean probability of these three sources to belong to samples of stars at their true 3-dimensional separations r_{S1} , r_{S2} , and r_{S8} - or larger - is even less than that. The value of P_{init} drops by a factor of 2 (i.e. to the FWHM value of that probability) at a mean radius of $r = 13.7 \text{ mpc}$ and by a factor of three at a radius of $r = 14.8 \text{ mpc}$. The probability of the stars to belong to samples at even larger radii lies well below 10%. We therefore adopted a value of about 15 mpc (0.4"). as a reasonable estimate of the radius of the volume that contains all three stars.

A *safe lower bound* to the size estimate of the volume described above is given by the upper limit of the projected separation of the stars from SgrA*. Of the three stars S8 has the largest projected separation from the center (see Tab. 2). Therefore we adopt 12 mpc (0.3") as a lower bound to the radius of the volume containing the three stars. This limit compares favorably with the size estimate derived above.

3.2. Enclosed mass estimates from accelerations

3.2.1. Correction of accelerations for projection effects

For a star at a projected separation R from the center and a total enclosed mass M one can calculate the projected, observable acceleration a_{obs} via

$$a_{obs} = GM \cos^3(\theta) R^{-2} \quad . \quad (4)$$

Here θ is the angle between the radius vector to the star and the plane of the sky containing the central mass. Plotting the lower limits $M \cos^3(\theta)$ of the enclosed mass as a function of the projected radius is equivalent to the assumption that the stars are in exactly the same plane of the sky as the central dark mass at the position of Sgr A*. This assumption is not justified and the approach does not answer the question of whether or not the observed projected accelerations are in agreement with the value and compactness of the enclosed mass derived at larger radii with different methods (Genzel et al. 2000, Ghez et al. 1998). A more realistic approach needs to correct for geometrical projection effects. A statistical estimate of M can be derived by using median values. As a consistent error estimate we use the median error defined as the median of the deviations of the individual estimates from their median. The quantity $(\cos\theta)^{-1}$ increases monotonically with the distance from the plane of the sky in which Sgr A* is located and its median can be calculated under the assumption of a stellar density distribution $n(r)$.

Using median values and a volume derived for a ensemble of stars make this method of correcting for geometrical effects much less susceptible to extreme correction values that occur for instance in the case of stars with large physical separations and small projected separations from SgrA* (i.e. θ approaching $\pi/2$). Contributions from those values would become dominant in case of a calculation of an expectation value for $(\cos\theta)^{-1}$ using $n(r)$ values as a weights.

3.2.2. Validity of the approach

In order to verify that the above described method results in acceptable statistically corrected enclosed mass estimates we performed simulations. The results of the de-projection procedure - presented in the $R - \log(M)$ -plane - show that the distribution of the de-projected mass estimate tends to under-estimate M for flat stellar distributions, whether the central mass is assumed to be point-like or extended, but is tightly peaked around the true value of M for steep cusp-like distributions.

We assumed a sphere with radius $r = 15 \text{ mpc}$ and a stellar number density $n(r)$ surrounding the dark mass of $3 \times 10^6 M_\odot$. For each star (we used several 1000) at a separation r from the center and a total enclosed mass M we calculated the projected radius R and the projected, observable acceleration a_{obs} via equation (4). In Fig. 5a,b,c we show the density of data points in the R - $\log M$ -plane for combinations of a central point mass (BH) or an extended central mass distribution and a constant or cusp-like stellar number density distribution. Almost all data points underestimate the enclosed mass M and the value

of that estimate drops dramatically towards smaller values of R . The density increase of data points towards larger projected distances from the center is due to the fact that the projection effects decrease for stars towards the projected edge of the limited volume. In Fig. 5d,e,f we correct both the projected radius R and the upper limit of the mass using the formalism outlined above in section 3.2.1. A higher density of points is located along the correct value of the enclosed mass and the remaining estimates are almost equally distributed above and below that value.

The available number density counts provide some evidence for an increased volume density of stars towards the center (Genzel et al. 2000, Alexander 1999, see also Alexander & Sternberg 1999). In Fig. 5b and Fig. 5e we have calculated the expected projected and statistically corrected mass estimates using a $r^{-7/4}$ stellar density law as an extreme case. The corrected mass estimates spread almost symmetrically about the expected value. At any projected radius the stellar number density along the line of sight is now biased towards the plane of the sky that contains SgrA*. This results in enclosed mass estimates that are less affected by the geometrical projection. For about 70% of all stars in Fig. 5b the projected enclosed mass estimate accounts for more than 70% of the true mass value. This demonstrates that for steep cusps the majority of the projected mass estimates will be much closer to the true value than in the case of a constant density distribution. For a $r^{-7/4}$ density law we would expect at least for two stars a mass estimate of at least $\sim 70\%$ of the enclosed mass. This is only barely fulfilled by S8 and S2. This shows, that a larger number of stars with significant curvature will greatly improve our knowledge on the presence and nature of a central stellar cusp.

3.2.3. Application to the measured data

In Fig. 6a we show projected mass estimates derived from the observed accelerations as a function of the projected radius listed in Tab. 1. In addition we indicate the mass distribution obtained from stellar and gas dynamics (for $R = 8.0$ kpc; see caption of Fig. 6 and Genzel et al. 2000, 1997, 1996, Eckart & Genzel 1996, 1997, Ghez et al. 2000, 1998).

As expected from the simulations presented in Fig. 5 the estimates obtained from S1 and S2 fall well below the enclosed mass estimate of $3 \times 10^6 M_\odot$ derived previously (see references above). For S8, however, (see discussion in section 4.2.2) and especially for S7, S10, S11 (not shown in Fig. 6a) - for which only *upper* limits of the acceleration could be obtained - the mass estimates are well above $3 \times 10^6 M_\odot$. For S7, S10, and S11 these *upper* limits range between $1.1 \times 10^7 M_\odot$ and $1.6 \times 10^7 M_\odot$. In Fig. 6b we show the mass estimates for S1, S2, and S8 as derived from the observed accelerations and corrected for projection effects following the method outlined in sections 3.2.1 and 3.2.2. The correction factors obtained for different volume sizes are listed in Tab. 4. The derived corrected radii and mass estimates are given in Tab. 5. The values cover a mass range of 2.9 to $7.2 \times 10^6 M_\odot$ over separations from Sgr A* between 8 and 15 *mpc*.

We compare the data to enclosed mass estimates as a function of separation from Sgr A* obtained assuming (physically not realistic) Plummer like density distributions (see discussion in Genzel et al. 1996, 2000) with a core radius r_c and a mass density $\rho(0)$ at the very center of the distribution. We chose the exponent $\alpha=5$, since this corresponds to the steepest currently observed drop in cluster mass density. For the stars S1 and S2 which are currently closest in projection to SgrA* the mean value and error of the enclosed mass corrected for a volume radius of about 15 *mpc* is $M_{acc} = (5 \pm 3) \times 10^6 M_\odot$. This value is fully consistent with an enclosed mass distribution that is flat down to radii of about 8 *mpc* with a value of $3 \times 10^6 M_\odot$ and a lower limit to the mass density of $3.7 \times 10^{12} M_\odot pc^{-3}$ for a core radius of $r_c = 5.8$ *mpc* as previously derived from the proper motion data (Genzel et al. 2000).

As is apparent from Fig. 6b this is the smallest range of true (not projected) separations from SgrA* for which a mass estimate corrected for projection effects has been derived so far. The fact that M_{acc} lies systematically above the enclosed mass obtained at larger radii can very likely be attributed to the fact that the volume size has been estimated correctly but the stars are systematically closer to Sgr A* along the line of sight than the median distance at the given projected radius (see Fig. 4). Alternatively, the estimate of the volume radius in which the two stars S1 and S2 are located is too large - which will result in the same effect and therefore in a correction that systematically over estimates the enclosed mass. Orbit calculations assuming a $3 \times 10^6 M_\odot$ point mass yield separations from the SgrA* plane of the sky of 6 – 7 *mpc* for S1 and S2. This indicates that for a volume radius of 15 *mpc* the described effect is in fact relevant.

Assuming a compact enclosed mass of $3 \times 10^6 M_\odot$ the range of derived mass estimates can also be used to qualitatively judge its compactness. For comparison we plotted in Fig. 6b the calculated Plummer like enclosed mass distributions for central mass density $\rho(0)$ and core radius values r_c of $10^{13} M_\odot pc^{-3}$ and 4.2 *mpc* and $10^{14} M_\odot pc^{-3}$ and 1.9 *mpc*, respectively. This comparison demonstrates that

- a) the estimates of the central enclosed mass and compactness derived from acceleration measurements for stars S1 and S2 are fully consistent with previously determined values (Genzel et al. 2000) and that
- b) under the assumption of a compact $3 \times 10^6 M_\odot$ central dark mass the current acceleration data allow central mass densities of $> 10^{13} M_\odot pc^{-3}$ and core radii of < 4 *mpc*. The star S2 currently (2000) is at a projected distance of only about 60 *mas* from the center. This is 4 times smaller than the minimum radius reached by the Jeans modeling (Genzel et al. 2000). If the orbit of S2 remains consistent with a compact mass of $3.0 \times 10^6 M_\odot$ the mass density is at least 64 times higher than the value based on the Jeans modeling i.e. $2.4 \times 10^{14} M_\odot pc^{-3}$. In this case the collapse life time of a hypothetical cluster of dark mass would shrink to only a few 10^6 years (Maoz 1998).

4. STELLAR ORBITS CLOSE TO Sgr A*

In the following we discuss possible Keplerian orbits for the three early type S-sources S1, S2, and S8 as well as two late type stars: S18 and star No.25 in Tab.1 by Genzel et al. (2000). In the following section 4.1 we first describe the algorithm we use to constrain the stellar orbits. In sections 4.2 and 4.3 we then apply it to the combined SHARP/NTT and NIRC/Keck data sets of the three high velocity stars S1, S2, and S8 and the two late type stars, respectively.

4.1. Orbit calculations

A complete global fit has to include the measurement errors of the relative positions and velocities given in Tab.2 and Tab.3, the uncertainties in the position of the central mass as well as its amount. In order to get a first insight into the stellar orbits we first restrict ourself to the case of a compact mass of $3 \times 10^6 M_\odot$ and a location of it that coincides with the nominal position of SgrA*. The influences of the uncertainties of these quantities on the 3-dimensional orbits will be discussed in section 4.3.

We have chosen to present the results of our simulations in the v_z - s_z -plane rather than the semi-major axes and eccentricity plane since this representation is closer to the observations. Progress in diffraction limited near-infrared spectroscopy now allows ongoing experiments to determine the line of sight velocity of the central stars. Calculated semi-major axes and eccentricities of the resulting orbits are listed in Tab.6. For two late type stars at the projected separations of about 0.5'' and 1'' from SgrA* radial and proper motion velocities are known. For these stars only the positions along the line of sight are undetermined. For the stars S1, S2, and S8 the line of sight velocities v_z and positions s_z are currently unknown. We considered orbits for the ranges of $-3500 < v_z < 3500 \text{ km s}^{-1}$ and $0 < |s_z| < 40 \text{ mpc}$. These intervals correspond to more than 5 times the central velocity dispersion and about twice the radius of the Sgr A* cluster and include all possible bound orbits. To judge the quality of the orbital fits we calculated reduced χ^2 values via

$$\chi^2 = \frac{1}{m - n} \sum \frac{(|\mathbf{x}(\mathbf{t}_i) - \mathbf{c}(\mathbf{t}_i)|)^2}{\sigma^2} . \quad (5)$$

Here $\mathbf{x}(\mathbf{t}_i)$ and $\mathbf{c}(\mathbf{t}_i)$ are the measured and calculated position vectors and σ the measurement uncertainties as a function of time, m is the number of observed data points and n the number of free parameters. We have used $n = 2$ since v_z and s_z are undetermined and currently the dominant source of uncertainty (see 4.3). The pairs v_z and s_z and $-v_z$ and $-s_z$ result in the same projected orbits and χ^2 values. Using the orbital data point that is closest to our reference position (see Tab.2) we synchronized the densely sampled calculated orbit with the measurements. In Fig.7 we show diagrams for the type for simulations described above. For the stars S1, S2, and S8 the resulting χ^2 values are shown

in the v_z - s_z -plane in Fig. 8, 10, and 12. In those diagrams we can in general distinguish between three areas labeled A, B, and C in Fig.7:

- A At small separations from Sgr A* ($s_z < 5 \text{ mpc}$) the calculated orbits have acceleration values which are well above what is measured. The corresponding χ_A^2 values are highest. These orbits can clearly be excluded.
- B At large separations from Sgr A* ($s_z > 10 \text{ mpc}$) or large line of sight velocities ($|v_z| > 2000 \text{ km/s}$) the orbits result in linear trajectories over the time interval from 1992 to 2000. The accelerations are too small. These orbital solutions can be excluded as well. Large χ_B^2 values in that region are due to the measurement uncertainties as well as a mismatch with respect to a straight line. This mismatch is due to the curvature in the measured orbital section.
- C Finally, there is an area in the v_z - s_z -plane in which the χ^2 values are lowest and correspond to acceptable orbital solutions with curvatures similar to what is measured. These minimum fit errors χ_C^2 are only dominated by the scatter in the data. The difference between χ_B^2 and χ_C^2 is a measure of the true χ^2 deviation of the measured curved orbital section from a simple linear trajectory - not contaminated by the scatter in the data.

In Fig. 7 we show the results of orbit calculations applied to simulated data for stars similar to S2. Compared to the available measurements these data have a similar sampling but are noise free with respect to the calculated orbits from which they have been drawn. The calculations show that the shape of the χ^2 minima depends on the orbital section for which measurements are available. Towards larger velocities and line of sight separations from SgrA*, i.e. lower orbital curvatures, it becomes increasingly difficult to distinguish between possible orbital solutions. The location of the minimum χ^2 values are smeared out towards this region. For a less curved section the line of sight separation can be higher to result in a similarly curved orbit section over the same amount of time and hence minimum χ^2 values at a higher velocity. Despite of this effect the simulations also show that a common intersection (marked with a filled circle in Fig. 7) of the regions of minimum χ^2 values remains at the correct v_z - and s_z -values with which the stellar orbits are launched at the corresponding epoch assumed for the simulations - excepting of course the ambiguity in the sign of those quantities (see section 1.1). How deep and close the absolute minimum of the χ^2 values is with respect to this location depends on the resolution (sampling in the v_z - s_z -plane) of the calculation, the signal to noise, and sampling of the observations.

To get a clear measure of the true χ_*^2 deviation of the measured curved orbital section from a simple linear trajectory - not contaminated by the scatter in the data - we corrected for both the SHARP/NTT and the NIRC/Keck data the χ^2 values by the corresponding minimum χ_C^2 values (see before).

$$\chi_*^2 = \chi^2 - \chi_C^2 \quad (6)$$

We then combined both data sets in a maximum likelihood (ML) analysis via:

$$\log(ML) = -\chi^2_{SHARP/NTT}/2 - \chi^2_{NIRC/Keck}/2. \quad (7)$$

The results are shown on the right hand side panels of Fig. 8 , 10, and 12 and discussed in the following section.

4.2. The central high velocity stars

In the previous section 4.1 we presented a general discussion of the procedure we use to match the data with Keplerian orbits. We now discuss detailed results for the individual stars obtained from the χ^2 fits in the v_z - s_z -planes and present characteristic orbits. We show that the high velocity stars S2, and most likely S1 and S8 as well are on bound, inclined ($60^\circ < i < 80^\circ$), and eccentric ($0.4 \leq e \leq 1.0$) orbits around a central, dark mass. For these 3 stars we list the 3-dimensional positions and velocities at the time averaged epoch of the current SHARP/NTT data set (1996.5) and the orbital elements derived from the combined SHARP/NTT and NIRC/Keck data sets in Tab.6. Our analysis also demonstrates that right now it is only the combination of the two sets that actually allows a first derivation of orbital elements.

4.2.1. Shapes of the orbits

S1 and S2: From the v_z - s_z -planes shown in Fig. 8 and Fig. 10 two classes of orbits can clearly be excluded. These are those with high curvature, corresponding to small distances to the plane of the sky in which SgrA* is located, as well as those orbits with small curvatures ($< 1 \text{ mas/yr}^{-2}$) and high eccentricities ($e > 1.0$). The orbital calculations reveal a well defined single χ^2 minimum. For star S1 about 80% of the $\log(ML)$ values within the 1σ contour in Fig. 8d correspond to eccentricities of $e \leq 1.0$ and the separation from the SgrA* plane of the sky is about $\sim 7 \text{ mpc}$. For star S2 *all* $\log(ML)$ values within the 1σ contours in Fig. 10 b) and d) are consistent with bound orbits, i.e. $e < 1.0$. Here both data sets (SHARP/NTT and NIRC/Keck) indicated separations from the SgrA* plane of the sky of $\sim 6 \text{ mpc}$ and a line of sight velocity in the range of $\pm 500 \text{ km/s}$. For both data sets and sources characteristic orbital solutions are shown in Fig. 9 and Fig. 11. For both stars the eccentricities are most likely in the range of $0.4 \leq e < 1.0$. For larger and smaller values of s_z the eccentricities and half axes become correspondingly larger and smaller (Tab. 6). For S2 the orbital elements listed in Tab.6 are defined best. For S1 about 20% of the orbital fits obtained from the possible v_z - s_z points (Fig.8d) result in large semi-major axes and high eccentricities.

S8: The v_z - s_z -planes are shown in Fig. 12 and for both data sets we show characteristic Keplerian orbits in Fig. 13 (see also Tab. 6). From Fig. 12, however, it is evident that there

is a clear mismatch between the measured curvature values and those indicated by the χ^2 minima. These minima show that pure Keplerian orbits result in a curvature of 0.6 to 0.8 $mas\ yr^{-2}$ rather than about 3 $mas\ yr^{-2}$ as obtained by the NTT and Keck proper motion experiments (see Tab.1). This mismatch corresponds to a 3-4 σ deviation from the measured value. The correspondence would be better for central masses above $3 \times 10^6 M_\odot$. However, already the lower enclosed mass limit derived from the accelerations of star S8 represents a 3-4 σ deviation from the values obtained via Jeans modeling and other mass estimations based on proper motions and Doppler velocities (see Tab.5 and Fig.6 in this paper and Tab.5 and Fig.17 by Genzel et al. 2000).

The orbital elements for S8 listed in Tab.6 correspond to the best fits to the data shown in Fig.1 in this paper and and Fig.1 in Ghez et al. (2000) and reproduce the observed time averaged positions and velocities but not the curvatures (see discussion in section 4.2.2). Orbits with large curvatures can clearly be excluded. The most probable eccentricities are just below $e \sim 1.0$. The proper motion velocity is too large for orbits with apoastron positions, i.e. regions of higher curvature closer to the present location of the star. This is a strong indication for the fact that the observed amount of curvature is not solely due to orbital motion. If this result is confirmed by further measurements consequences are that S8 cannot be used to pinpoint the location of SgrA* (see section 2.2).

Influence of the position and amount of the central mass: The errors of the orbital elements in Tab.6 have been derived from the uncertainties of the 3D-positions and velocities listed below. Since the possible range of v_z and s_z that results from our fit is large compared to the measurement uncertainties of the proper motion velocities and positions (see Tab.2) the resulting uncertainties on the orbital elements are much smaller and well covered by their errors listed in Tab.6.

The $\pm 30\ mas$ (Menten et al. 1998) uncertainty of the position of SgrA* - which we assume to be associated with the central mass - is comparable to the uncertainty of the line of sight separation s_z . It amounts, however, to only less than about 1/8 of the 3-D separation of the stars from SgrA*. A simultaneous variation of the amount and position of the central mass within the $\pm 30\ mas$ and the $(2.6-3.3) \times 10^6 M_\odot$ intervals shows that the orbital elements in Tab.6 represent a solution at the global χ^2 minimum of the orbital fits to the measured data. We find that such a variation of the position and amount of the central mass causes changes in the eccentricities and the semi-major axes that are well covered by the errors of the orbital elements given in Tab.6. Therefore the main result - that the central stars are on fairly inclined and eccentric orbits - is independent of the variation of the involved quantities within their errors.

4.2.2. What causes the acceleration of S8 ?

In the previous section we have shown that the orbital curvature observed by both proper motion experiments is too large for being solely due to Keplerian motion. We now discuss a variety of reasons that could explain the observed acceleration of the star S8.

Stellar scattering: The curvature of S8's orbit corresponds to a deviation from a straight line by an angle ψ . If this is caused by a scattering star of mass m , then its distance r_s from S8 is given by

$$r_s \sim 2G(m_{S8} + m)/(v_\infty^2 \psi) \quad (8)$$

(Binney & Tremaine 1994), where v_∞ is the relative velocity at infinity between the two stars. The probability of such a scattering event occurring during the time Δt of the monitoring campaign is

$$P = \pi r_s^2 n v_\infty \Delta t \approx 4\pi G^2 n (m_{S8} + m)^2 \Delta t / (v_\infty^3 \psi^2), \quad (9)$$

where n is the stellar number density. Here $v_\infty \sim \sigma_{central} \sim 500$ km/s corresponds to the velocity difference of both stars at large separations. The mass of S8 is assumed to be $m_{S8} \sim 15 - 20 M_\odot$ (Eckart, Genzel, Ott 1999, Genzel et al. 1998). This implies $m' = (m_{S8} + m) \sim 20 M_\odot$ for $m \leq 1 M_\odot$. With the central stellar mass density given by (Genzel et al. 1998, 2000) we assume that the stellar number density is of the order of $n \sim 10^6$ pc⁻³. From the acceleration values in Tab.1 we derive an observed scattering angle ψ of the order of 20 degrees for S8. Equation 9 can then be written as

$$P \approx 5 \times 10^{-8} \times n [10^6 \text{ pc}^{-3}] (m' [20 M_\odot])^2 (v_\infty [500 \text{ km/s}])^{-3} \quad (10)$$

This shows that even if the stellar number density is higher by a few orders of magnitude due to a stellar cusp or if v_∞ varies by a few 100 km/s the scattering probability is always very low.

Flux density of neighboring stars: A K=15-17 background or foreground star close to the current line of sight toward S8 could also be responsible for a positional shift that gives rise to the observed apparent acceleration. However, S8 has moved by about 160 mas over the past 8 years. At a wavelength of 2 μm this corresponds to the angular resolving power of the NTT and about 3 times the resolving power of the Keck telescope. Such a star near S8 has not yet been reported but - if present and not strongly variable - should be detected soon. If the S8 acceleration is due to such a star the S8 trajectory should straighten again in the near future.

Alternatives: If other observational biases (e.g. misalignments in position or position angle) were relevant one would expect even larger variations in proper motions at increasing projected separations from the center. These variations are not observed in both independent data sets. Also a systematical underestimation of the enclosed mass from proper motions and radial velocities is not likely. See detailed discussions in Genzel et al. (2000). A lensing event can also be excluded as a straightforward explanation for the observed acceleration. For stars as bright as S8 such events are very unlikely and result in a flux density increase over a period of approximately 1 year (Alexander & Loeb 2001,

Alexander & Sternberg 1999). Within less than about 0.5 magnitudes S8 was constant in flux density over the past 8 year.

As a conclusion the acceleration of S8 that has been detected in both the SHARP/NTT and the NIRC/Keck experiment is either due to a flux contamination of an unrelated object along the same line of sight or due to a rare scattering event in the dense environment of the central stellar cluster.

4.2.3. Other central early type stars

For the remaining early type stars of the central Sgr A* cluster positions and proper motions are known (Genzel et al. 1997, Ghez et al. 1998, Ghez et al. 2000, Genzel et al. 2000). Orbit calculations show that stars in the Sgr A* cluster with line of sight separations from the center of $s_z < 30$ mpc and line of sight velocities v_z smaller than 2 to 3 times the velocity dispersion of the central arcsecond will be on bound orbits around the black hole. A more detailed analysis, however, still awaits a detection of their orbital curvature and/or their radial velocity.

4.3. Late type stars at small projected separations

There are two stars with prominent CO band head absorption that are located at small projected separations from SgrA* and for which the full 3-dimensional velocity information is available. The corresponding v_z - s_z -planes and characteristic orbital solutions are shown in Fig. 14. It cannot be fully excluded that these stars are at small physical distances to the center. Our orbital analysis, however, shows that the current data suggest a likely location outside the central 0.3 pc diameter section of the Galactic Center stellar cluster which is dominated by the early type He-stars. In the following we discuss the results of our orbital analysis for both stars.

*No.25 - 0.43"E; 0.96"S of SgrA**: Based on R~5000 VLT ISAAC observations Eckart, Ott,& Genzel (1999) report the presence of a late type star with strong $2.3\mu\text{m}$ CO band head absorption about 1" south of the center. We identify this object with the K=12.4 proper motion star No.25 in Tab.1 of Genzel et al. (2000) and star S1-5 in Tab.1 by Ghez et al. (1998). This star is located at a projected separation of 1.05" about 0.43"E and 0.96"S of SgrA*. This star is approximately 0.3 magnitudes brighter than the overall southern part of the SgrA* cluster (containing S9, S10, S11, and a few $K \geq 16$ stars just E of S10 and S11). In a 0.3"-0.5" seeing under which the VLT data (Eckart, Ott, Genzel 1999) were taken the flux density contribution of this star in a 0.6" NS slit is comparable to that of the southern part of the SgrA* cluster. A fainter star almost exactly 1.1"S of SgrA* can be excluded as a possible identification of the late type star, since its brightness is about 0.3 magnitudes fainter than the individual stars S11 or S10 and hence almost a full magnitude

fainter than the total of the southern part of the SgrA* cluster. The wavelength calibration of the R~5000 VLT ISAAC data - as well as a comparison to the spectrum of the late type star IRS14SW (see Tab.1 by Genzel et al. 2000) that fell into the NS oriented slit and was acquired simultaneously - indicate a line of sight velocity of the star 0.43" E and 0.96" S of SgrA* of -80 ± 40 km/s. The SHARP/NTT proper motion data of this object including the results of the 1999 and 2000 observing run are shown in Fig.2 and listed in Tab.3. A comparison of the radial and proper motion velocities indicates that this star is on a predominantly tangential orbit in the plane of the sky.

In Fig.14 we investigate the possible orbital solutions that lead to bound orbits. The thick (red) continuous and dashed lines mark line of sight separations from SgrA* for which the eccentricities $e < 1$. About 60% of the possible current line of sight separations are located beyond the radius within which the He-stars dominate the emission. About 30% even lie beyond the core radius of the central stellar cluster of ~ 0.3 pc. If the line of sight separations s_z are of the order of 150 to 200 mpc the eccentricities are smaller than unity and the semi-major axes of the orbits will be of the same order as s_z . These numbers are lower limits only, since they are derived for simple Keplerian orbits under the assumption of a dominant central mass of $3 \times 10^6 M_\odot$. For orbits with eccentricities (as calculated for the simple Keplerian case in Fig.14) closer to $e = 1.0$ and values for $s_z > 200$ mpc the orbits will have large (several degrees) Newtonian periastron shifts. The stars reach true physical separations from the center of well beyond 1.0 pc for which the mass of the stellar cluster starts to dominate. Under these conditions bound stellar orbits with line of sight separations larger than what is indicated by the thick (red) lines are possible.

*S18 - 0.04" W; 0.45" S of SgrA**: This star is listed as S18 in Tab.1 of Genzel et al. (2000) but not contained in the corresponding list of Ghez et al. (1998). Its most recent SHARP/NTT proper motion data are listed in Tab. 3. Based on deep CO(2-0) line absorption Gezari et al. (2000) identify this object as an early K-giant which is blue shifted with respect to the Galactic Center stellar cluster at about -300 km/s. Of all late type stars in the central stellar cluster S18 has the smallest angular separation ($< 0.5''$) from SgrA* reported to date. A comparison of the radial and proper motion velocities indicates that this star could be on a predominantly radial orbit. In Fig.14 we investigate the possible orbital solutions that lead to bound orbits. The thick (red) continuous and dashed lines mark line of sight separations from SgrA* for which the eccentricities $e < 1$. About 50% of the possible current line of sight locations are located beyond the radius of the He-stars cluster and reach out to the core radius of the central stellar cluster. For the reasons mentioned above bound stellar orbits with line of sight separations larger than what is indicated by the red lines are possible.

Highly eccentric orbits like those labeled with 'I' in Fig.14 bring both late type stars physically too close to the position of SgrA*. These orbits can be excluded because for a black hole mass of $3 \times 10^6 M_\odot$ the tidal disruption radius for a giant is

$$R_t \sim 1.2 \text{ mas} \times (R_*/10^{12} \text{ cm}) \times (M_*/M_\odot)^{1/3} \quad (11)$$

(e.g. Frank & Rees 1976, Binney & Tremaine 1994), where R_* and M_* are the giant’s radius and mass. For orbits with semi-major axes of $a \sim 20 \text{ mpc} \sim 0.5''$ and eccentricities of $e > 0.94$ every giant will be destroyed on its periastron passage. The coupling between the orbit and the tides raised on the star will cause deviations from a point mass behavior even at separations larger than R_t . Correspondingly this would allow only wider orbits for giants. Along the same line of arguments equation 11 also provides additional evidence that the central high velocity stars (the S-stars) are O-stars rather than late type giants. This identification, however, still awaits spectroscopic confirmation.

5. SUMMARY AND CONCLUSIONS

The combination of the high precision but shorter time scale NIRC/Keck data with the lower precision but longer time scale SHARP/NTT data set allows us to have a first insight into the nature of *individual* stellar orbits as close to the massive black hole at the center of the Milky Way as currently possible.

We have shown that a statistical correction for geometrical projection effects allows us to derive an enclosed mass estimate from the observed accelerations of stars S1 and S2 of $M_{acc} = (5 \pm 3) \times 10^6 M_\odot$. This value is fully consistent with an enclosed mass that is flat down to radii of about 8 mpc with a value of about $3 \times 10^6 M_\odot$ and mass density of $3.7 \times 10^{12} M_\odot \text{ pc}^{-3}$ for a core radius of $r_c = 5.8 \text{ mpc}$ as derived from the proper motion data (Genzel et al. 2000). Our most recent data - compared to and combined with published data on proper motions and accelerations (Ghez et al. 2000, Genzel et al. 2000, Eckart et al. 2000, Ghez et al. 1999, Ghez et al. 1998) - show that S2 - and most likely S1 and S8 as well - are on orbits around a central, dark, and massive object coincident with the position of the radio source SgrA*. The stars are on bound fairly inclined ($60^\circ < i < 80^\circ$) and eccentric ($0.4 < e < 0.95$) orbits. In Fig.15 we show for star S2 right ascension and declination as a function of time as predicted from our analysis of the combined data set. The analysis is in agreement with the result by Genzel et al. (2000) that the central stars are preferentially on eccentric orbits. This statement also holds for S8 - just taking into account its velocity at the current projected position - although it is likely that not the entire amount of its measured acceleration is due to orbital motion.

Properties of a possible cusp: The current kinematical data on individual central stars make it difficult to accommodate a high density cusp with a stellar density law as steep as $n(r) \sim r^{-7/4}$. In section 3.2.2 we have shown that for steep cusps the majority of the projected mass estimates is much closer to the true value than in the case of for instance a constant density distribution. For three stars randomly picked out of a cluster following a $r^{-7/4}$ density law we would at least for two stars expect that the mass estimate derived from their accelerations accounts for $\sim 70\%$ of the enclosed mass. With S8 and possibly S2

this is just barely the case for the Galactic Center. The presence of a pronounced stellar cusp within the central few 100 mpc would make that area collisionly dominated and most of the stars would be expected on parabolic orbits (Alexander 1999). Our orbit calculations show that the current data of both the SHARP/NTT and NIRC/Keck experiment clearly indicate that the central stars are on bound and not on parabolic orbits. This weakens the case for a *strong* cusp and suggests that the stellar density is not high enough to provide a collisionally dominated environment.

Due to the limited number of detected stars a minimum radius of 10 mpc (0.25") is currently used for the determination of the mass and mass density from proper motion measurements. The $\alpha=5$ Plummer like model of a dark cluster results in a core radius of such a hypothetical cluster of $r_{core}=5.8$ mpc (0.15") and corresponding central density of $3.7 \times 10^{12} M_{\odot} \text{ pc}^{-3}$. The statistical correction for geometrical projection effects presented in section 3.2 shows that the acceleration data of the two closest stars S1 and S2 are in agreement with such a compact mass. Accepting the correction for the most likely volume that contains S1 and S2 - the data would even be fully consistent with a core radius of $r_{core}=4.2$ mpc (0.17") and corresponding central density of $10^{13} M_{\odot} \text{ pc}^{-3}$. If the trajectory of S2 remains consistent with an orbit around a compact mass of $3.0 \times 10^6 M_{\odot}$ the lower limit for the mass density that can be derived from this stellar orbit may be as large as $2.4 \times 10^{14} M_{\odot} \text{ pc}^{-3}$. In this case the collapse life time of a hypothetical cluster of dark mass would shrink to only a few 10^6 years (Maoz 1998).

Two late type stars for which proper motion and radial velocities are known, and that are at projected separations of about 0.5" and 1.0" from SgrA* are very likely at larger physical distances from the center and part of the larger scale central stellar cluster with a core radius of approximately 0.3 pc. Our analysis indicates that the strong curvature of the available orbital section of star S8 is possibly due to either a flux contamination by an unrelated object along the same line of sight or a result of a rare scattering event in the dense environment of the central stellar cluster.

The analysis of stellar orbits (Ghez et al. 2000, Genzel et al. 2000, Eckart et al. 2000, and this paper) clearly supports the presence of a compact dark mass at the position of SgrA*. The VLBI maser nucleus of NGC 4258 (Greenhill et al. 1995, Myoshi et al. 1995) and the dark mass at the center of the Milky Way are currently the best and most compelling cases for the existence of super-massive nuclear black holes (Maoz 1998).

Future developments: Future observations at higher sensitivity and angular resolution will allow us to find and track the motion of stars that are even closer, i.e. < 4 mpc, to the center than those currently accessible. Orbital time scales at the resolution limit of the VLT, LBT, or Keck interferometer could be in the range of a few months. A detection of a relativistic or Newtonian periastron shift would ultimately result in a direct determination of the compactness of the enclosed central mass (Rubilar & Eckart 2000; see also Fragile & Mathews 2000). Measurements of the prograde relativistic or the retrograde Newtonian

orbital periastron shifts are within reach of current and upcoming instrumentation.

We are thankful to the ESO Director General and his staff to let us bring the SHARP camera to the NTT in 1999 and 2000. We thank Reiner Hofmann and Klaus Bickert for their help with SHARP at the NTT. We are also grateful to the NTT and La Silla team for their interest and technical support of the SHARP camera.

REFERENCES

- Alexander, T., Loeb, A., 2001, ApJ 551, 223
- Alexander, T., 1999, ApJ 527, 835
- Alexander, T., Sternberg, A., 1999, ApJ. 520, 137
- Backer, D.C. 1996, Proc. of the 169th Symp. of the IAU, p.193
- Binney, J., & Tremaine, S. 1994, Galactic Dynamics, Princeton Univ. Press, Princeton, U.S.A.
- Bowers, R., & Deeming, T., 1984, Astrophysics, Jones and Bartlett Publishers, London, U.K.
- Eckart, A., Ott, T., Genzel, R., 2001a, IAU 205, Proc. of IAU Symp. NO.205 on "Galaxies and Their Constituents at the Highest Angular Resolutions", p.41., Dordrecht:Reidel.
- Eckart, A., Ott, T., Genzel, R., Rubilar, G., 2001b, in "Science with the LBT," Proceedings of a workshop held at Ringberg Castle, Tegernsee / Germany 24-29 July 2000, Tom Herbst (ed.), Neumann Druck, Heidelberg, Germany, ISBN 3-00-008071-6
- Eckart, A., Ott, T., Genzel, R., 1999, A&A, 352, 22
- Eckart, A., Genzel, R., 1997, MNRAS 284, 576
- Eckart, A., Genzel, R., 1996, Nature 383, 415
- Figer, D., et al. 2000, ApJ 533, 49
- Fragile, P.C., & Mathews, G.J., 2000, ApJ 542, 328
- Frank, J., & Rees, M.J., 1976, MNRAS 176, 633
- Genzel, R., Pichon, C., Eckart, Gerhard, O.E., Ott, T., 2000, MNRAS 317, 348
- Genzel, R., et al. 1996, ApJ 274, 153
- Genzel, R., Eckart, A., Ott, T., Eisenhauer, F., 1997, MNRAS 291, 219
- Gerhard, O., ApJ 546, L39
- Gezari, S., Ghez, A.M., Becklin, E.E., Larkin, J., McLean, I., & Morris, M., 2000, A.A.S. Meeting 197, #04.01
- Ghez, A. M., Klein, B. L., Morris, M., Becklin, E. E. , 1998, ApJ 509, 678
- Ghez, A., Morris, M., Becklin, E.E., Kremenek, T., Tanner, A., 2000, Nat. 407, 349
- Greenhill, L. et al. 1995, ApJ 440, 619
- Haller, J.W., Rieke, M.J., Rieke, G.H., Tamblyn, P., Close, L., Melia, F., 1006, ApJ 468, 955
- Jaroszyński, M., 1998, Acta Astronomica, 48, 653
- Klein, B., Ghez, A.M., Morris, M., Becklin, E.E., 1996, ASP Conf. Vol. 102
- Krabbe A. et al., 1995, ApJ, 447, L95

- Leonard P. J. T., Merritt D., 1989, ApJ 339, 195
- Maoz E., 1998, ApJ, 494, L13
- Menten, K.M., Reid, M.J., Eckart, A., Genzel, R., 1996, ApJL 475, L111
- Munyanza, F., Tsiklauri, D., Viollier, R.D., 1998, ApJ 509, L105
- Myoshi M., et al., 1995, Nature, 373, 127
- Reid M. J., Readhead A.C.S., Vermeulen R.C., Treuhaft, 1999, ApJ, 524, 816
- Rubilar, G.F. & Eckart, A., 2001, A&A 374, 95
- Sellgren K., McGinn M.T., Becklin E.E., Hall D.N.B., 1990, ApJ, 359, 112

TABLES

Table 1: Accelerations

		SHARP			Keck	
	$d_{Sgr\ A^*}$	a_α	a_δ	$a_{1996.5}$	$d_{Sgr\ A^*}$	$a_{1995.53}$
source: S1	3.10 ± 0.12	$+1.5 \pm 1.7$	-3.5 ± 1.8	3.8 ± 2.4	3.44 ± 0.03	2.4 ± 0.7
S2	5.37 ± 0.12	$+1.0 \pm 0.7$	-2.1 ± 0.6	2.3 ± 0.9	4.61 ± 0.04	5.4 ± 0.3
S8	13.7 ± 0.12	-3.3 ± 0.7	-0.3 ± 0.9	3.3 ± 1.1	14.64 ± 0.04	3.2 ± 0.5
S7	24.5 ± 0.12			< 3.0		
S10	17.8 ± 0.12			< 4.0		
S11	21.9 ± 0.12			< 3.0		
S18	17.5 ± 0.12			< 3.0		
No.25	40.7 ± 0.15			< 3.0		

Projected separations d from SgrA* in *mpc* and stellar accelerations a in units of $mas\ yr^{-2}$ ($1.203 \times 10^{-3} m\ s^{-2}$) for the SHARP/NTT (1996.50) and NIRC/Keck (1995.53) data. For the SHARP/NTT data we also give R.A. and Dec. acceleration components a_α and a_δ from which the total orbital acceleration $a_{total} = (a_\alpha^2 + a_\delta^2)^{1/2}$ has been derived.

Table 2: Positions

	SHARP		Keck	
epoch	1996.5		1997.6	
	$\Delta\alpha$	$\Delta\delta$	$\Delta\alpha$	$\Delta\delta$
source: S1	-0.080	-0.020	-0.083	-0.037
S2	-0.010	+0.142	-0.012	+0.121
S8	+0.320	-0.170	-0.338	-0.189
S18	-0.040	-0.450	-0.037	-0.443
No.25	+0.430	-0.960	-	-

Positions relative to SgrA* in *arcsec* for the mean center epochs of 1996.5 (SHARP) and 1997.6 (Keck) as derived from our own data and the data presented by Ghez et al. (2000). The assumed relative 1σ errors are 10 mas (SHARP) and 5 mas (Keck, Ghez et al. 2000), respectively. For star No.25 and S18 data are taken from Genzel et al. (2000). Keck data for S18 are taken from Gezari et al. (2000).

Table 3: Proper Motion Velocities

	SHARP		Keck	
	v_α	v_δ	v_α	v_δ
S1	+541±60	-1460±60	+568±60	-1528±60
S2	-290±60	-694±60	-271±60	-733±60
S8	+535±60	-552±60	+472±60	-558±60
S18	+3 ±60	146±60	-	-
No.25	-227±60	14±60	-	-

The velocities in $km\ s^{-1}$ were obtained for epochs 1996.5 (SHARP) and 1997.6 (Keck) via interpolation of the measured velocities for epochs 1996.5 (SHARP) and 1995.4 (Keck) with the measured projected accelerations in R.A. and Dec. (see Tab 1). For S18 a radial velocity of $v_z = -300$ km/s is given by Gezari et al. (2000), and for No.25 a radial velocity of -80 km/s is derived from ISAAC VLT data (this paper and Eckart, Ott, Genzel, 1999). For errors see caption to Tab. 7.

Table 4: Correction Factors

	r_V [arcsec]	S1		S2		S8	
		$\cos(\theta)$	$\cos(\theta)^{-3}$	$\cos(\theta)$	$\cos(\theta)^{-3}$	$\cos(\theta)$	$\cos(\theta)^{-3}$
Keck							
	0.3	0.54 ±0.17	6.44±5.1	0.67 ±0.17	3.4 ±2.2	1.0	1.0
	0.4	0.42 ±0.15	13 ±12	0.54 ±0.17	6.4 ±5.0	0.99 ±0.07	1.02 ±0.02
	0.5	0.35 ±0.13	24±22	0.45 ±0.16	11 ±9	0.93 ±0.07	1.26 ±0.23
SHARP							
	0.3	0.50 ±0.17	8.3 ±6.9	0.73 ±0.16	2.5 ±1.4	1.0	1.0
	0.4	0.39 ±0.14	17 ±15	0.61 ±0.18	4.5 ±3.3	0.97 ±0.02	1.08 ±0.07
	0.5	0.32 ±0.12	32 ±29	0.51 ±0.17	7.5 ±6.1	0.90 ±0.08	1.36 ±0.32

The geometrical correction factors have been calculated for a constant number distribution $n(r)$ of stars within the central volume in the potential of a central compact mass as indicated by current observations (see equation (33) and Tab.5 by Genzel et al. 2000).

Table 5: Corrected Mass Estimates

	S1		S2		S8	
	radius	mass	radius	mass	radius	mass
	[mpc]	[$10^6 M_\odot$]	[mpc]	[$10^6 M_\odot$]	[mpc]	[$10^6 M_\odot$]
SHARP	8.0 ± 2	6.4 ± 3.8	9.0 ± 1.6	2.9 ± 1.5	14.4 ± 0.8	6.2 ± 1.0
Keck	8.1 ± 2	3.7 ± 2.1	8.6 ± 1.7	7.2 ± 3.8	15.2 ± 0.5	6.7 ± 0.8

Here we used the correction factors for a flat stellar distribution listed in Tab.4.

Table 6: Orbital parameters

source	S1	S2	S8
i [°]	60^{+5}_{-5}	70^{+6}_{-17}	0^{+70}_{-70}
ω [°]	190^{+120}_{-10}	190^{+10}_{-10}	-55^{+32}_{-0}
Ω [°]	-14^{+7}_{-12}	23^{+27}_{-11}	~ -65
e	$0.6^{+0.30(*)}_{-0.30}$	$0.8^{+0.15}_{-0.40}$	$0.95^{+0}_{-0.12}$
a [mpc]	$18^{+18(*)}_{-8}$	$5.6^{+0.7}_{-1.1}$	10^{+48}_{-0}
T [yrs]	$2097^{+281(*)}_{-96}$	$2002.6^{+6.8}_{-2.2}$	2043^{+1060}_{-0}
P [yrs]	$100^{+184(*)}_{-54}$	$19.4^{+7.4}_{-3.0}$	57^{+1060}_{-0}
s_α [mpc]	-3.02 ± 0.19	-0.38 ± 0.19	$+12.10 \pm 0.19$
s_δ [mpc]	-0.76 ± 0.19	$+5.38 \pm 0.19$	-6.43 ± 0.19
s_z [mpc]	$+7 \pm 1$	$+6 \pm 1$	< 4
v_α [km/s]	$+541 \pm 60$	-290 ± 60	$+535 \pm 60$
v_δ [km/s]	-1460 ± 60	-694 ± 60	-552 ± 60
v_z [km/s]	-400^{+800}_{-300}	0 ± 500	0 ± 1000

Top: Orbital elements for the stars S1, S2, S8 as derived from the combined SHARP/NTT and NIRC/Keck data sets (see Tab.6). We listed the orbital elements for the orbits labeled 'I' in Figs.8-13. The uncertainties correspond to the variation of orbital elements within the 1σ contour of Figs.9, 11, and 13. The orbital elements for S2 are defined best. For S1 we have listed the orbital parameters for the $\sim 80\%$ of the fit areas within the 1σ contours with eccentricities below $e = 0.9$. In the remaining $\sim 20\%$ of the cases the quantities marked with an asterisk may become significantly larger. These orbits for S1 may even be not bound.

We listed the inclination i , the sky position angle ω of the periastron position, the sky position angle Ω of the northern most knot (transition between dashed and solid sections of the orbits in Figs.8, 10, and 12), as well as the eccentricity e and semi-major axes a of the deprojected orbits, and finally the year T of the periastron transition and the orbital period P . Future spectroscopic measurements have to determine the sign of the inclination i as well as which of the knots is the ascending one. The errors are derived from the uncertainties of the 3D-positions and velocities listed below.

Bottom: 3D-positions and velocities at the mean center epochs of 1996.5 as derived for the SHARP/NTT data. The range of line of sight separations s_z and velocities v_z result from the combined SHARP/NTT and NIRC/Keck data sets. The s_z and v_z pairs are uncertain by a common sign factor of ± 1 .

FIGURE CAPTIONS

Fig. 1.— Positions of the stars S1, S2, S8, S7, S10, and S11 relative to the position of SgrA* as a function of the SHARP/NTT observing epoch from 1992 till 2000. For the stars S1, S2, S8 we show parabolic variations of the positions that correspond to the data presented in the text and in Tab.1. For the other stars for which only upper limits of the curvature were derived we show linear fits. The declination velocity plot has been shifted by +300 mas.

Fig. 2.— Positions of the two late type stars No.25 (0.43" E; 0.96" S) in Tab.1 by Genzel et al. (2000) and S18 (0.04" W; 0.45" S) relative to the position of SgrA* as a function of the SHARP/NTT observing epoch from 1992 till 2000. The data shows no indication for significant orbital curvature above a value of about 3 mas yr^{-2} . The declination velocity plot has been shifted by +300 mas.

Fig. 3.— The position of the central dark mass derived from the SHARP/NTT and NIRC/Keck acceleration data of S1 and S2. For the stars S1 and S2 the measured acceleration data corresponds well to curvature values expected from orbital motion around a central dark mass.

The grey shading is proportional to the probability of the location of the central dark mass, i.e. the maximum likelihood score given in the text. The smaller probability plot for the combined SHARP/NTT-NIRC/Keck acceleration data has been inserted into the probability plot derived from the SHARP/NTT data alone. The central filled dashed circle marks the radio position of SgrA* and corresponding uncertainties of ± 30 mas. The thin contour lines indicate limit at which the $\log(ML)$ -score drops by a factor of 0.5 below its maximum. The α and δ coordinates of the central mass can be read off from the projections of the thin contour lines at the 68.4% and from the thick contour line at the 90% level. The time averaged positions of the SHARP/NTT and NIRC/Keck data as well as the error cones of the acceleration data for S1 and S2 are indicated by different symbols explained in the figure legend. For the NIRC/Keck we have taken the error cone widths used in Fig.2 of Ghez et al. (2000) rather than those implied by the values in their Tab.1. The positional uncertainties for the SHARP and NIRC positions have been included in the grey scale plot and the width of the cones.

Fig. 4.— Relevant quantities to correct the measured accelerations of stars near the Galactic center for projection effects.

Fig. 5.— Enclosed masses as a function of projected and true separation from SgrA* derived from observed stellar acceleration data for different distributions $\rho(r)$ of the central compact dark mass and the surrounding stars $n(r)$ within the central volume of 0.4" (15 mpc) radius. The top three images (a-c) show the lower limits of the enclosed mass from observed accelerations. The bottom three images (d-f) show the enclosed mass from accelerations statistically corrected for projection effects. The left two graphs assume a $3 \times 10^6 M_\odot$ point mass and a constant number density of stars. The two graphs in the middle assume a $3 \times 10^6 M_\odot$ point mass and a $r^{-7/4}$ number density of stars. The two graphs to the right

assume an extended central mass distribution $\rho(r)$ and a constant number density of stars. Contour lines are at 5, 10, 20 and 50% of the peak density of data points.

In all panels we also show the mass estimates obtained via Jeans modeling (indicated by the open box) and other mass estimations (grey shaded box) based on proper motions and Doppler velocities (see Fig.17 by Genzel et al. 2000).

Fig. 6.— Enclosed masses calculated from observed orbital accelerations.

a) Lower limits for the enclosed mass estimates from the projected accelerations. The data points are labeled with source names and origin of the measurements. The sizes of the error bars are dominated by the uncertainties in the determination of the accelerations. We plotted the SHARP/NTT data as derived for the mean observing epoch. In the case of the NIRC/Keck data we used the quantities given in Table 1 of Ghez et al. (2000).

b) Mass estimates with the statistical correction for geometrical projection effects described in the text. The data points represent the estimates for a volume radius (see text section 3.2) of $0.4''$ (15 mpc). Data points and labels for the individual sources have been enclosed in a dotted line. The area shaded in light grey includes the enclosed mass estimates corrected for central volume radii ranging between $0.3''$ (11 mpc) and $0.5''$ (19 mpc). The corrected mass estimates have been derived for a constant number distribution $n(r)$ of stars within the central volume in the potential of a central compact mass consistent with current observations (see equation (33) and Tab.5 by Genzel et al. 2000). See text for further explanation.

In both panels we also show the mass estimates obtained via Jeans modeling (indicated by the open box) and other mass estimations (grey shaded box) based on proper motions and Doppler velocities (see Fig.17 by Genzel et al. 2000).

Fig. 7.— Orbital fit calculations applied to simulated data on a star similar to S2. The calculations were carried out for two data sets of the same orbit. The results of the calculations are shown on the left, the corresponding orbits on the right. The simulations show that the shape of the distribution of minimum χ^2 values (inverted grey scale shading and corresponding contour lines) is a function of the orbit section to which the calculations are applied (see text for explanations). For comparison we have plotted the contour line representation of the results for the two orbital sections in both v_z - s_z -planes on the left. The filled circle marks the common intersection of the regions of minimum χ^2 values at the position of the 'true' current line of sight separation and radial velocity of the star - excepting of course the ambiguity in the sign of those quantities. The asterisk denotes the position of the central mass.

Fig. 8.— Orbital fits for the star S1.

a) The reduced χ^2 values calculated from the 1992 to 2000 SHARP/NTT measurements and orbits computed from the data in Tab. 2, Tab. 3 and the corresponding line of sight velocities and separations from SgrA*, as given by the labels of the axes. The χ^2 values are represented in an inverted grey scale and by the labeled thick contour lines (see equation 5). Thin contour lines represent the eccentricities e of the corresponding orbits. All points within the $e = 1.0$ contour lines represent bound orbits. The $e = 0.5$ contour is shown as a dashed line.

b) The grey scale plot shows the likelihood score (see text) derived via the χ^2 values from the SHARP/NTT and the NIRC/Keck data shown in panel a) and c). A continuous black contour line indicates the 1σ limit at which the $\log(ML)$ score drops by a factor of 0.5 below its maximum. Roman numbers label the positions of representative best fit orbits within this contour. The projections of the corresponding orbits onto the plane of the sky is shown in Fig. 9. The calculated accelerations a are represented by thick contour lines with labels in units of $mas\ yr^{-2}$. Thin contour lines represent the orbital eccentricities e . The $a = 0.5\ mas\ yr^{-2}$ and $e = 0.5$ contours are shown as dashed lines.

In panels **c)** and **d)** we show the corresponding information for the NIRC/Keck data (Ghez et al. 2000). While the grey scale likelihood plot is the same in panels **b)** and **d)** the labeled contour lines represent the eccentricities and accelerations obtained from the orbit calculations only using the SHARP/NTT and the NIRC/Keck data, respectively.

Fig. 9.— Selected Keplerian orbits with velocities and separations from SgrA* for star S1 as given by the data in Tab. 2 and Tab. 3. The orbit labels correspond to those in Fig. 8b and Fig. 8d. The orbits represent the range of best fits (within the 1σ contour line in Fig. 8; see text) to the 1992 to 2000 SHARP/NTT data (crosses) and the 1996 to 1999 NIRC/Keck data (crosses also marked by thin lines on either side of the orbital tracks; Ghez et al. 2000). The dashed lines indicate those sections of the orbits that are - with respect to the current position of the stars - on the opposite site of the plane of the sky SgrA* is located in (see also caption of Tab.6). The projected position of SgrA* is indicated by an asterisk.

Fig. 10.— Orbital fits for the star S2. See caption of Fig. 8 and description in text.

Fig. 11.— Selected Keplerian orbits for S2. See caption of Fig. 9.

Fig. 12.— Orbital fits for the star S8. See caption of Fig. 8 and description in text. The orbital fits reveal a mismatch between the measured curvature values of about $3\ mas\ yr^{-2}$ and those resulting from best fit pure Keplerian orbits of 0.6 to $0.8\ mas\ yr^{-2}$.

Fig. 13.— Selected Keplerian orbits for S8. See caption of Fig. 9.

Fig. 14.— Possible orbital solutions and selected projected orbits for the two late type stars No.25 ($0.43''E$; $0.96''S$) and S18 ($0.04''W$; $0.45''S$). For panels **a)**, **c)** and **b)**, **d)** see captions of Fig. 8 and Fig. 9, respectively. The thick (red/grey) lines indicate the range in line of sight velocity and separation from SgrA* for which bound orbits are possible (see comment on lower limits in text). For the thick dashed line the velocities and separations have to be multiplied by -1. The orbits IV are not shown. For $0.43''E$; $0.96''S$ orbit IV is close to an EW flip of orbit III and for S18 orbit IV is close to an NS flip of orbit III.

Fig. 15.— Prediction of position time plots for different possible orbits of the star S2. For a line of sight separation from the plane of the sky containing Sgr A* of $s_z = 6$ mpc the following line of sight velocities have been used (see section 4 and Fig.11): I: $s_v = 0$ km/s; II: $s_v = -500$ km/s; III: $s_v = +500$ km/s. The longest orbital time scales suggested by the

current data correspond to orbits with $s_z = 7$ mpc and a : $s_v = -500$ km/s or b : $s_v = 500$ km/s. The SHARP/NTT data is shown as well. The declination velocity plot has been shifted by +300 mas.

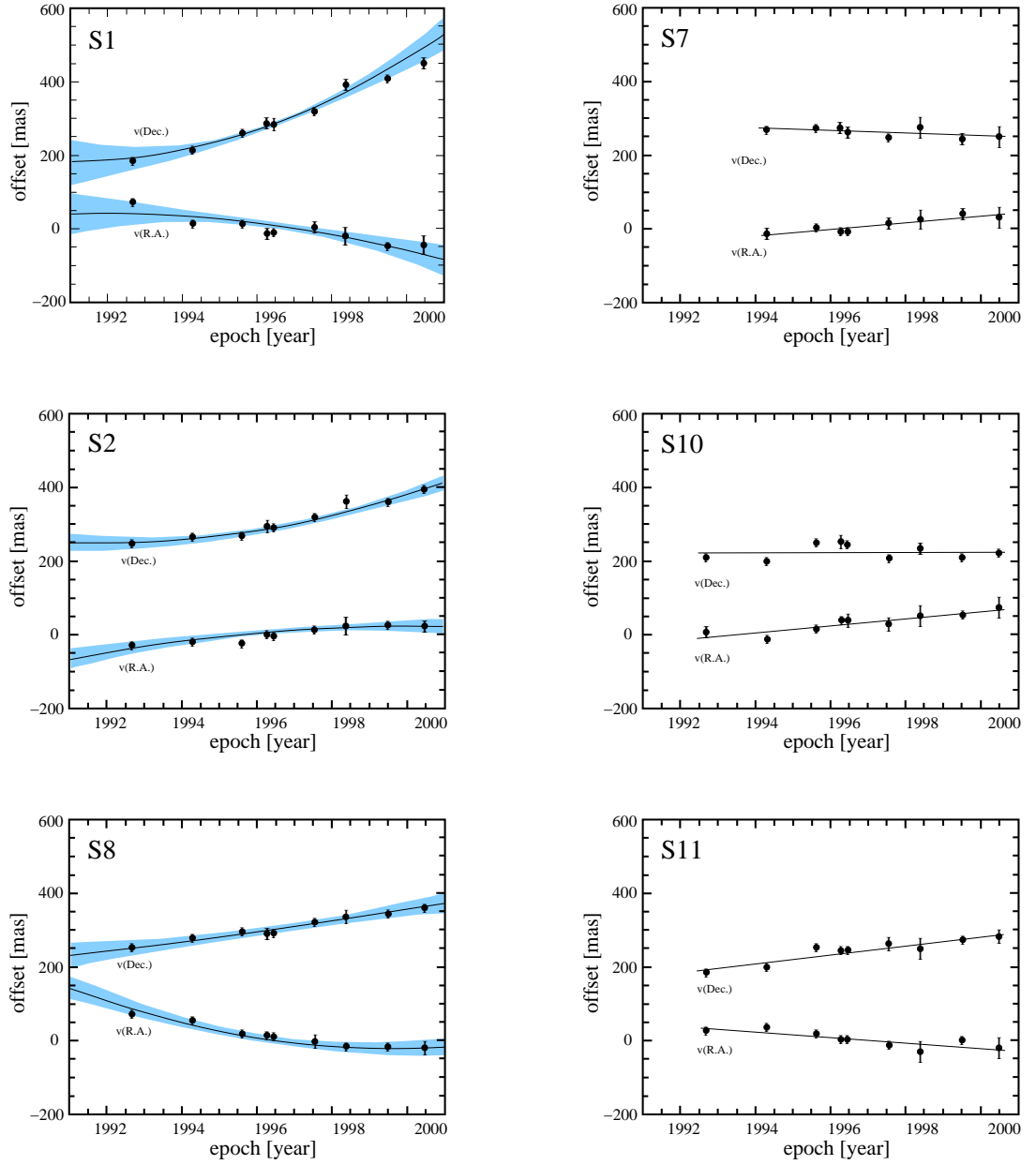


Fig.1

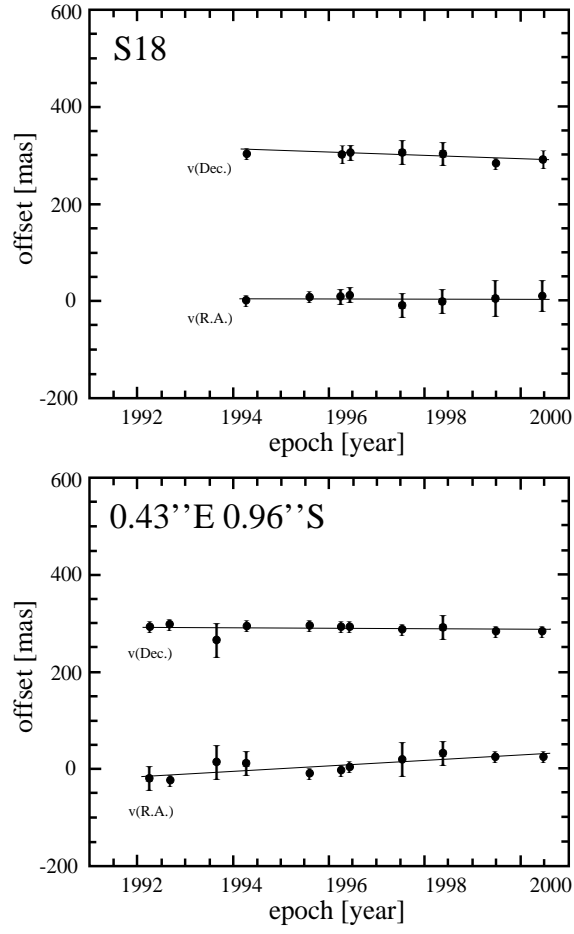
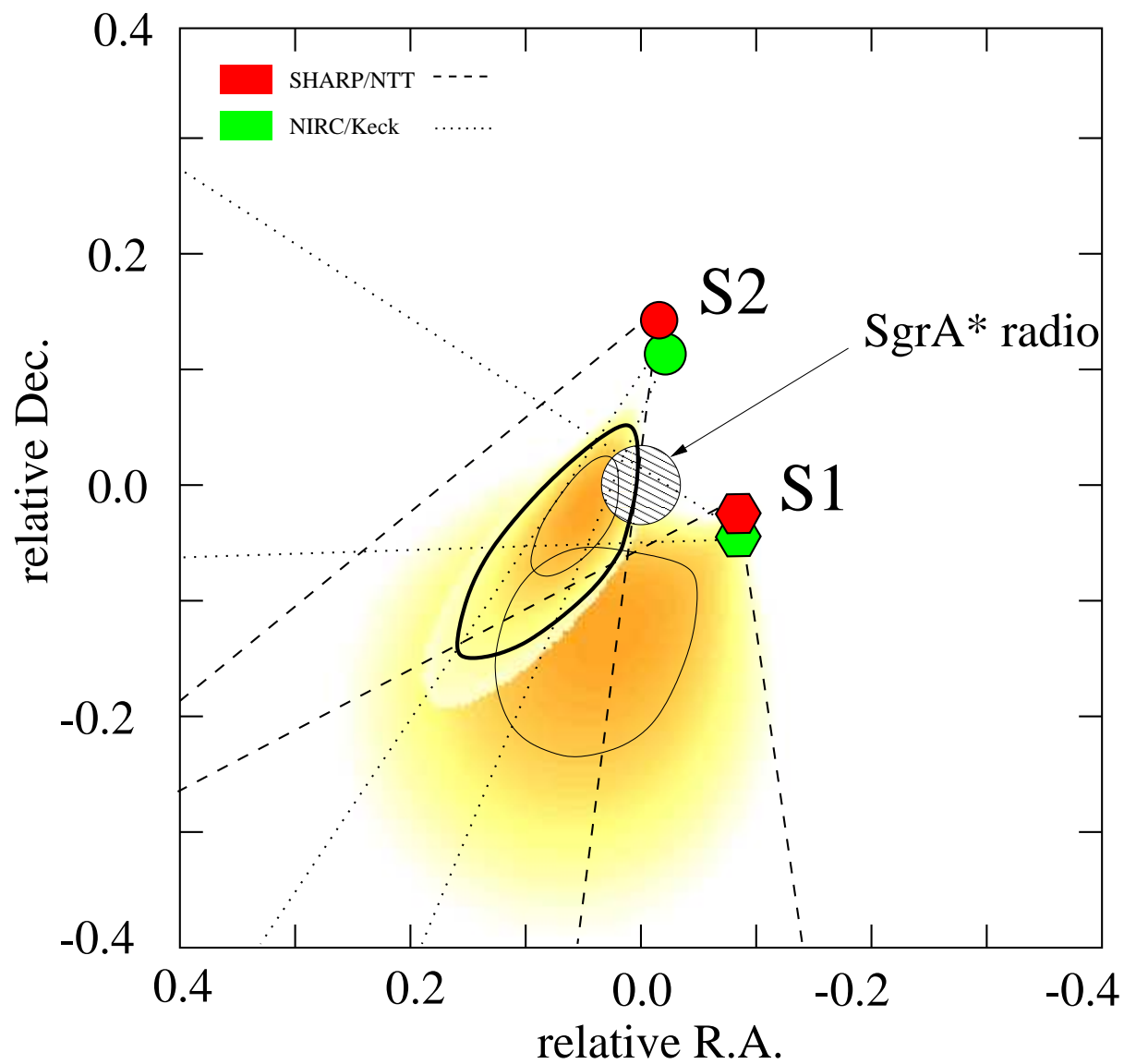


Fig.2



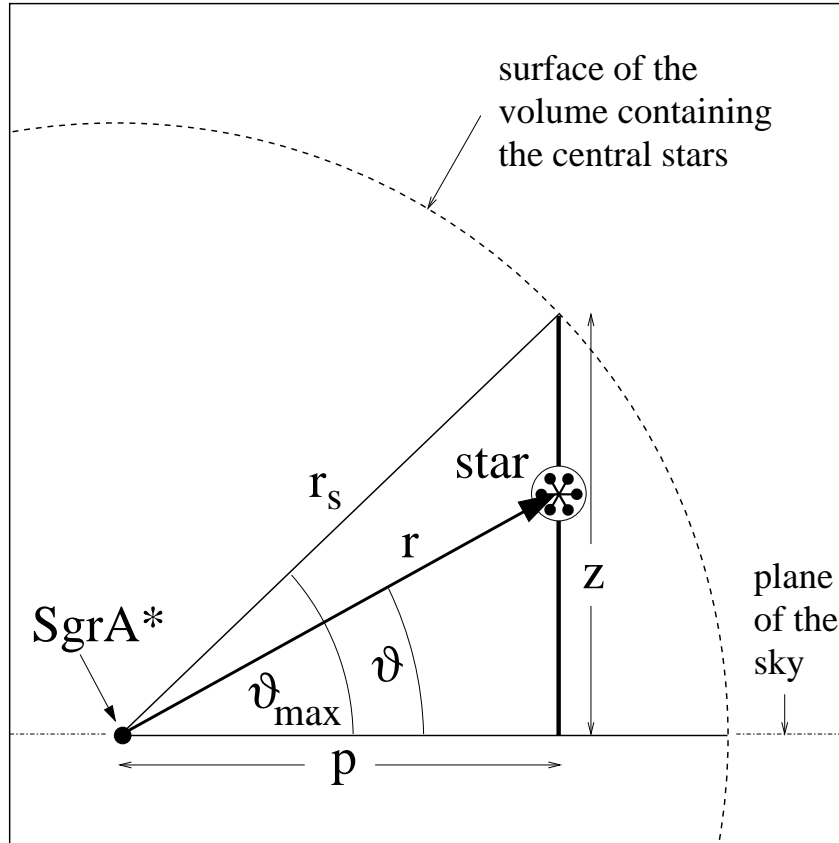


Fig.4

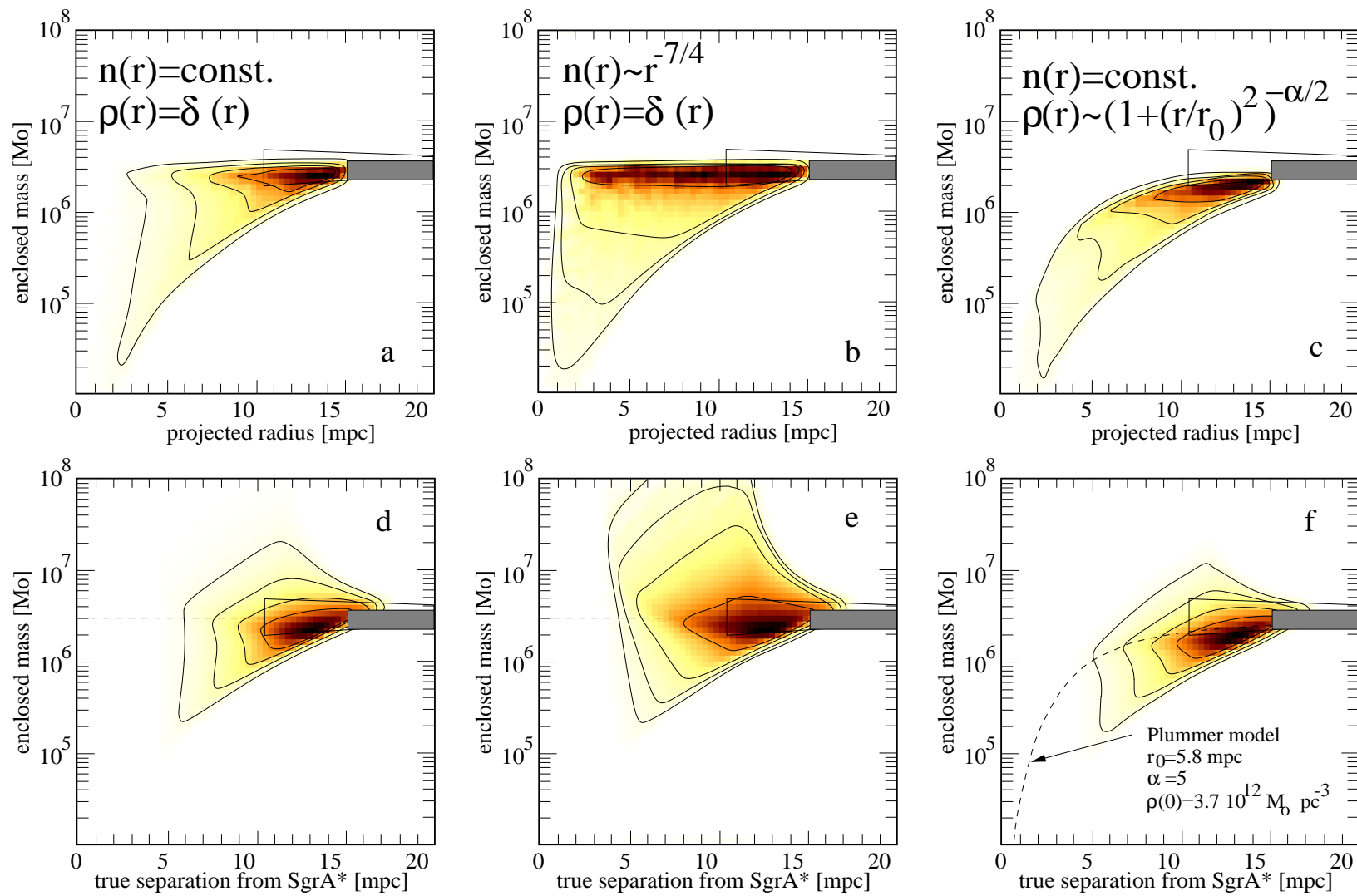


Fig.5

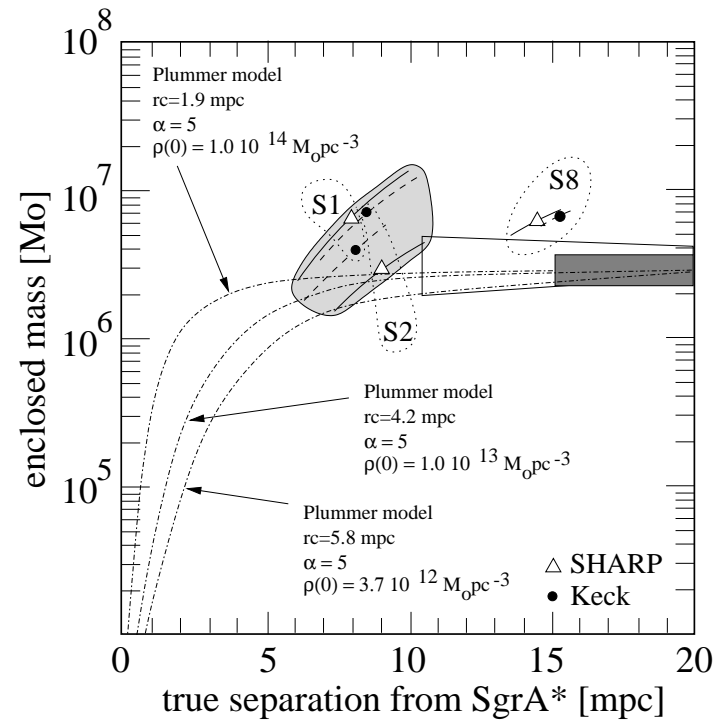
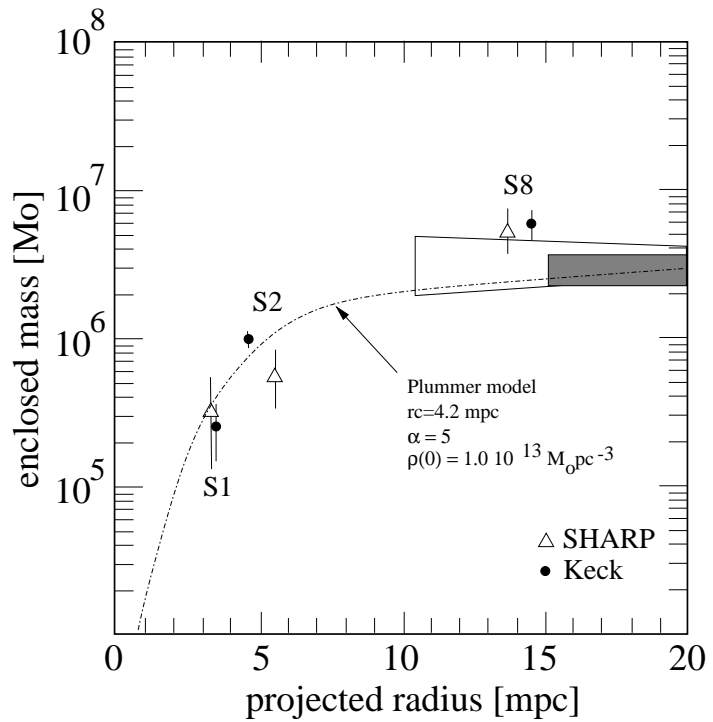


Fig.6

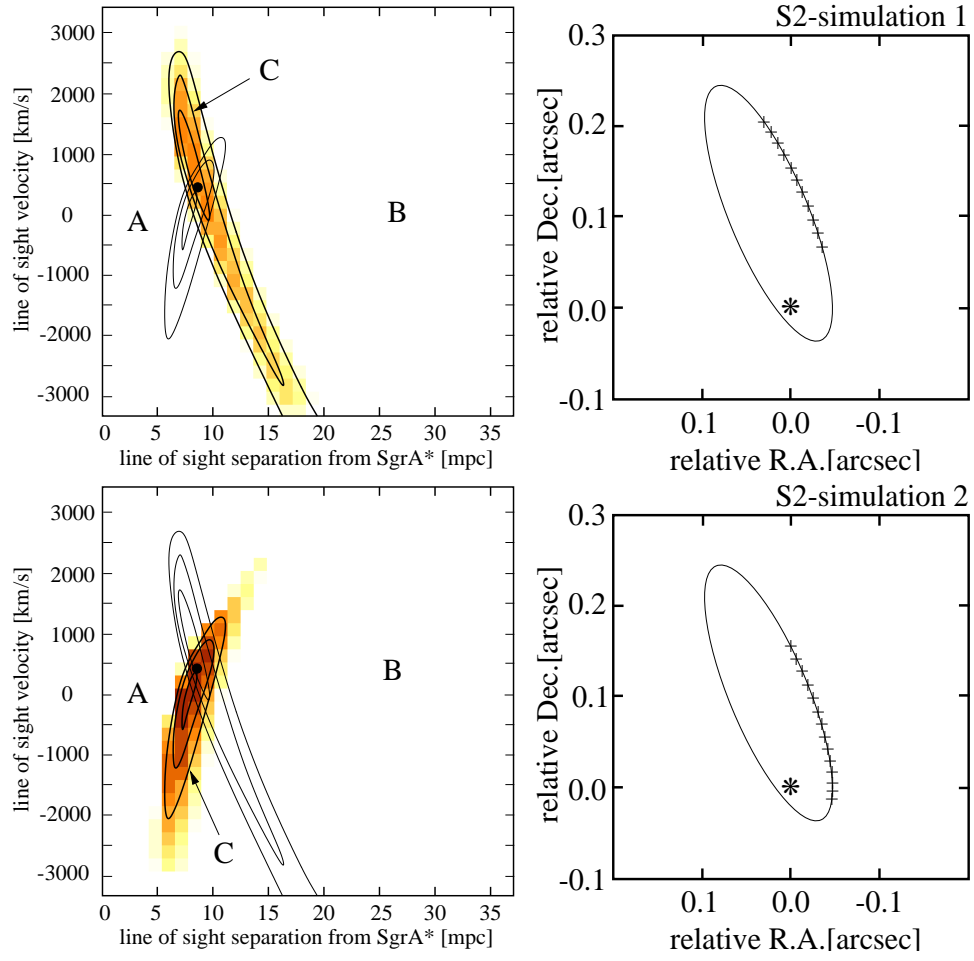


Fig.7

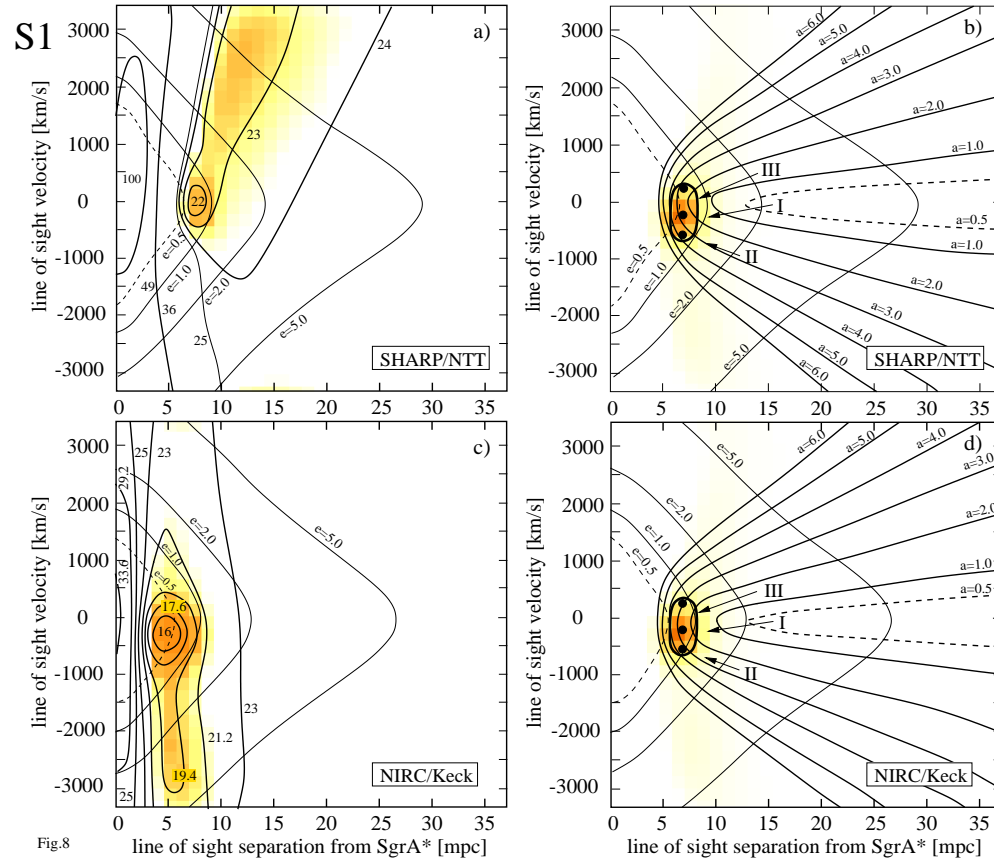


Fig.8

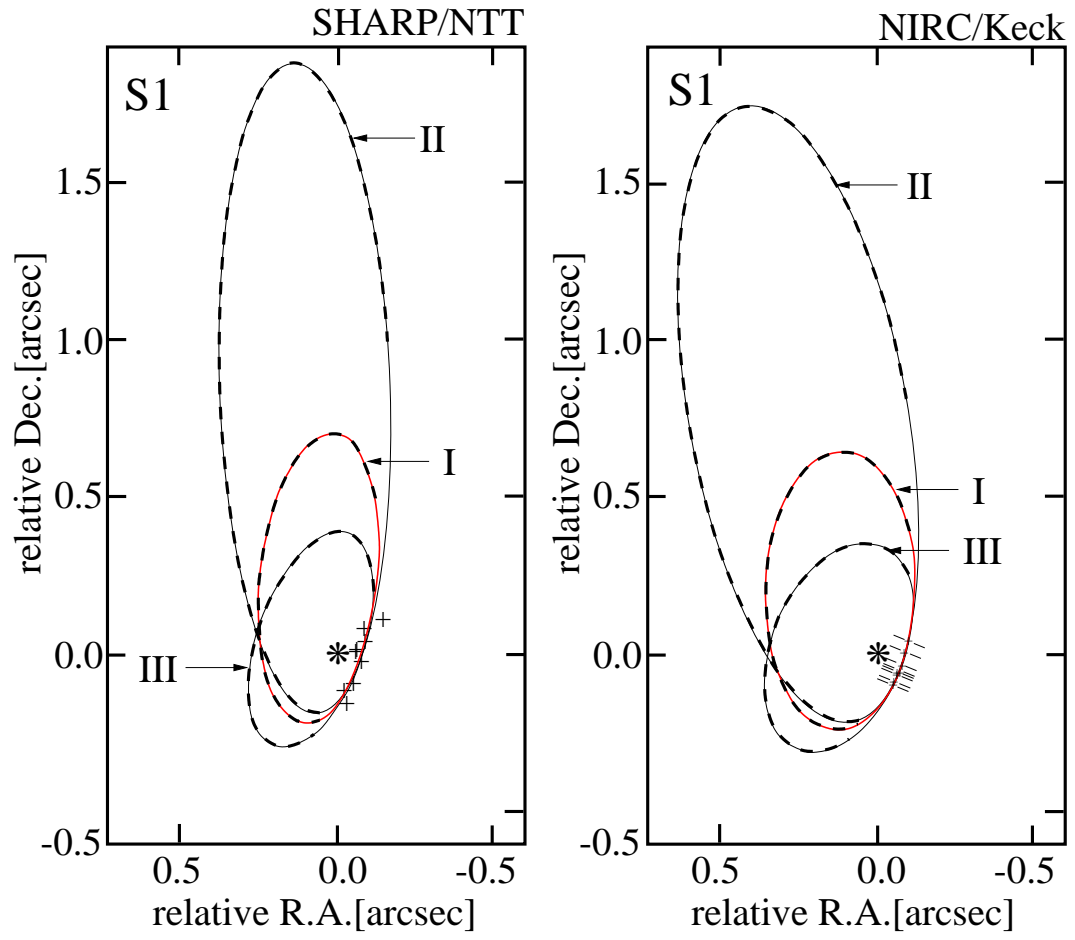


Fig.9

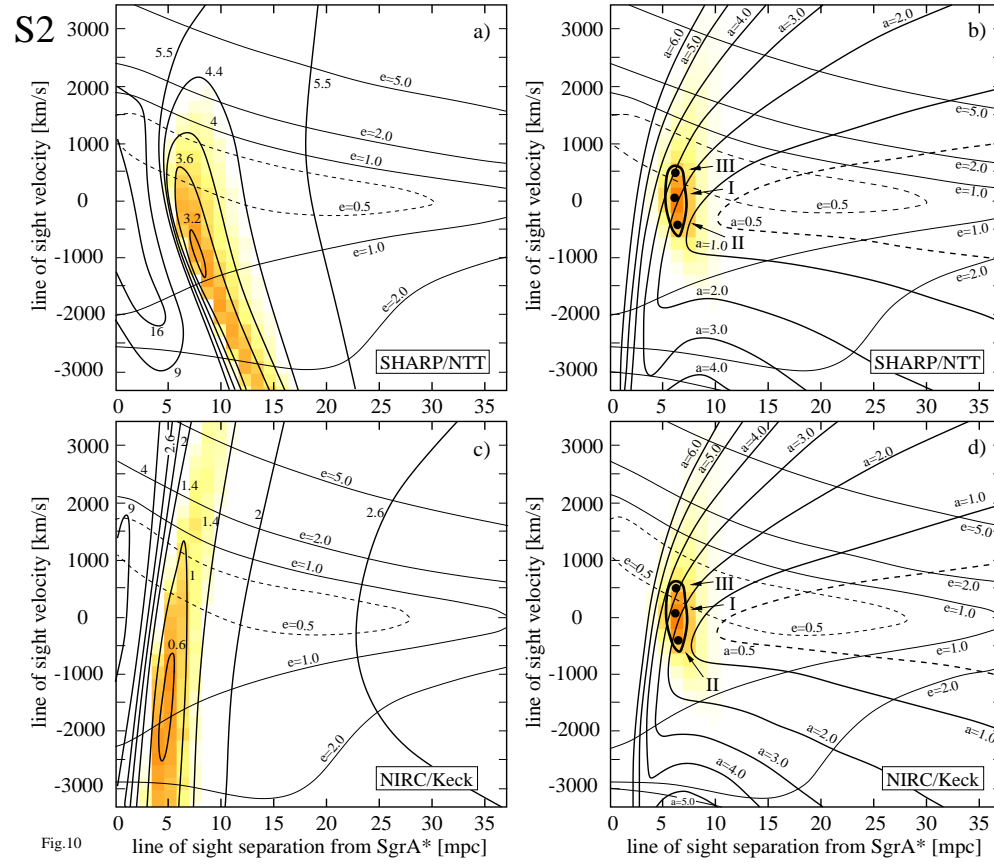


Fig.10

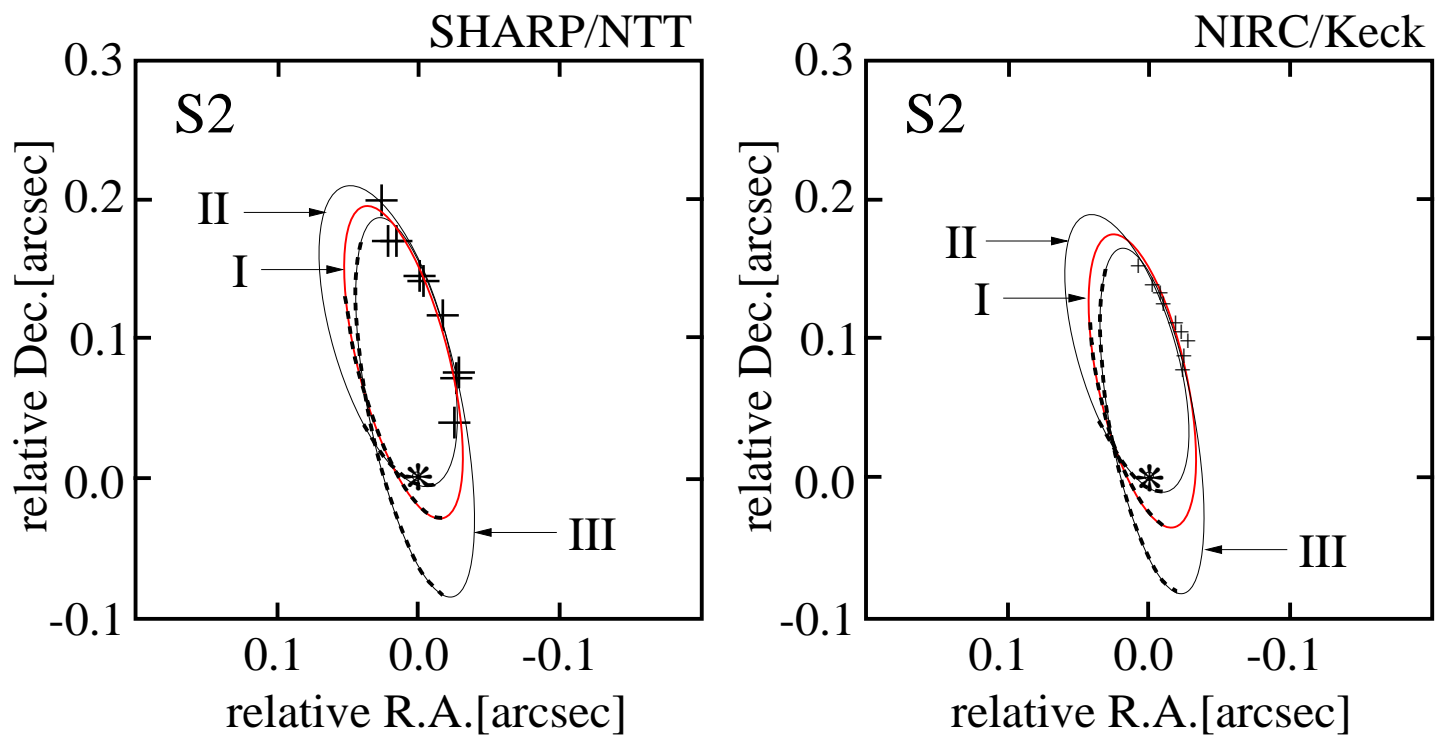
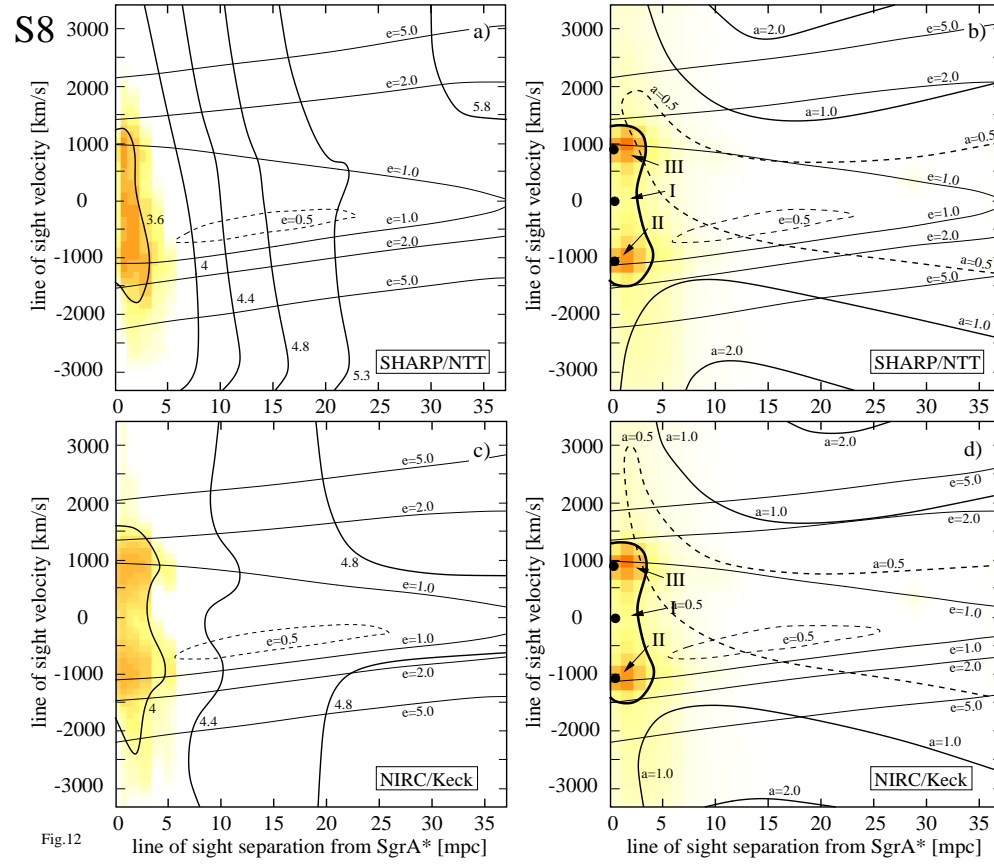


Fig.11



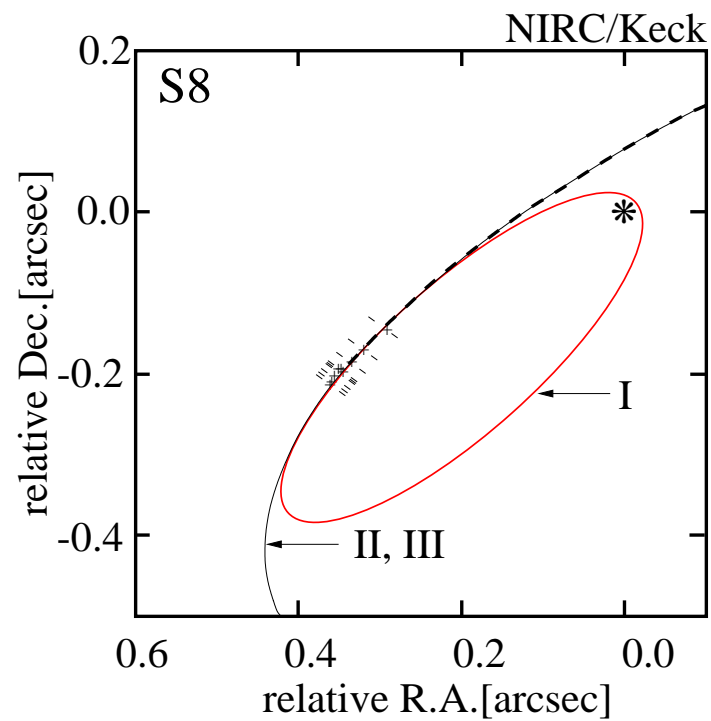
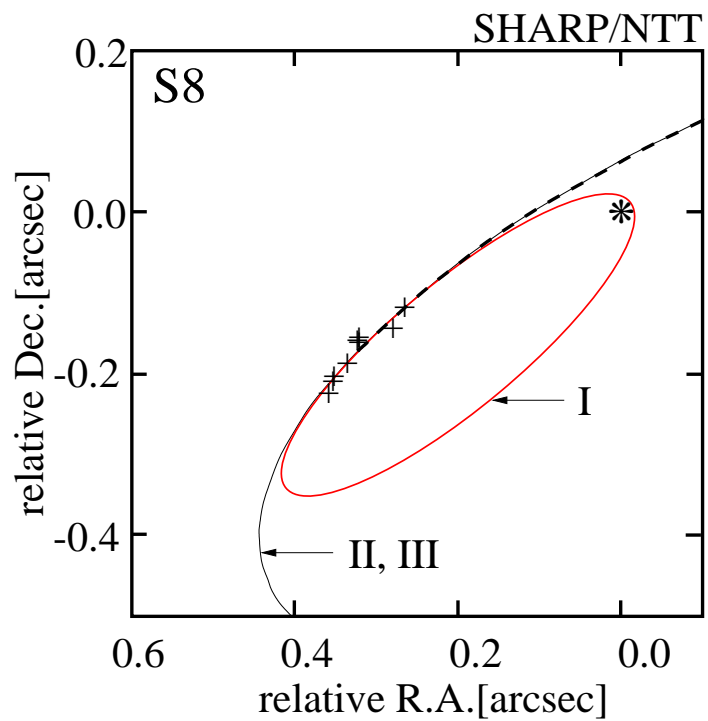


Fig.13

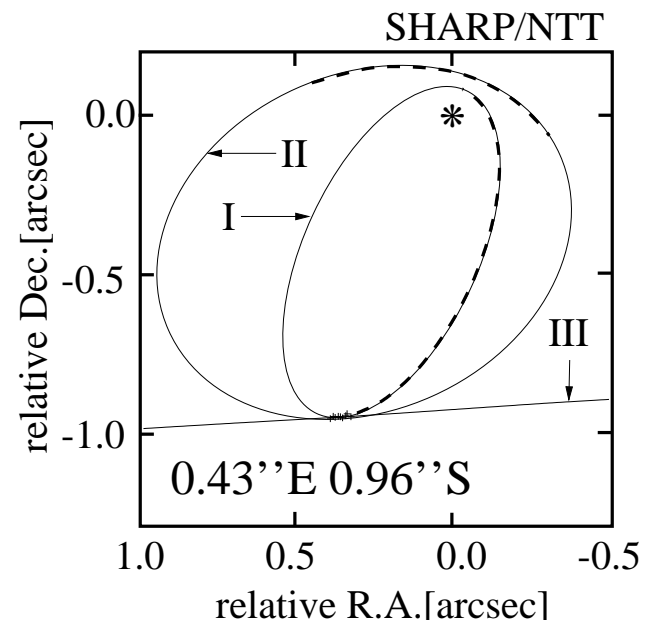
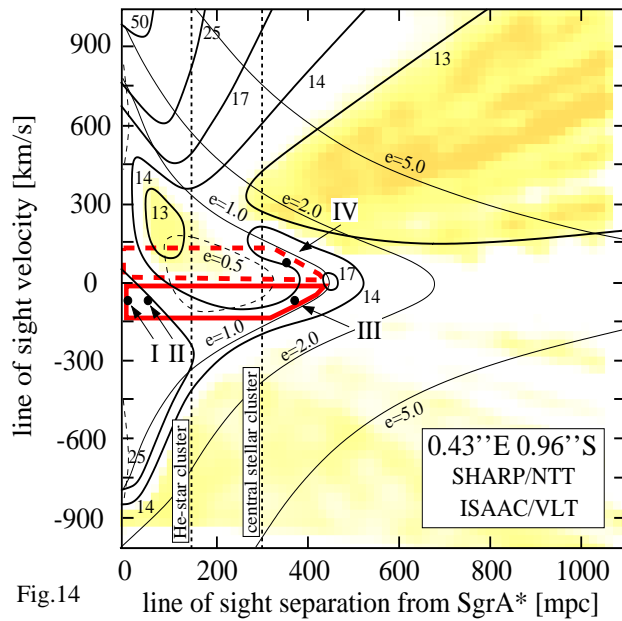
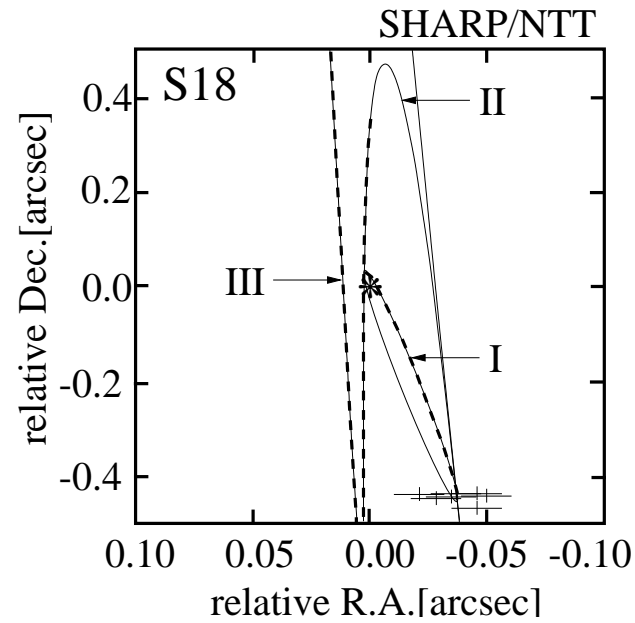
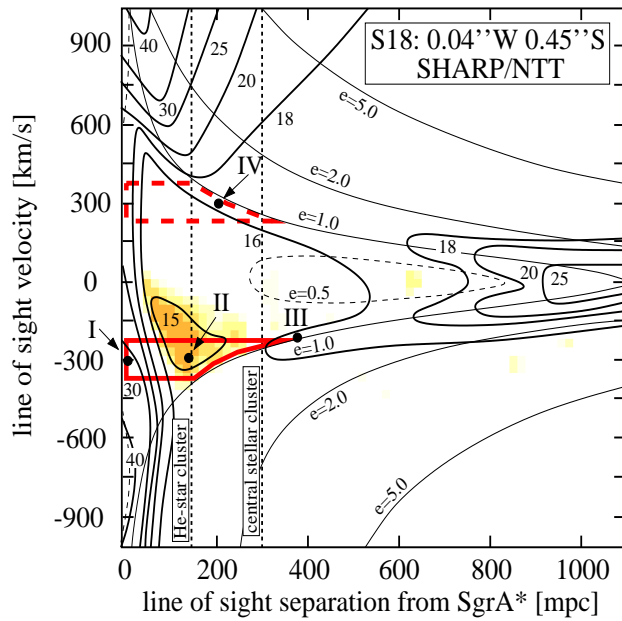


Fig.14

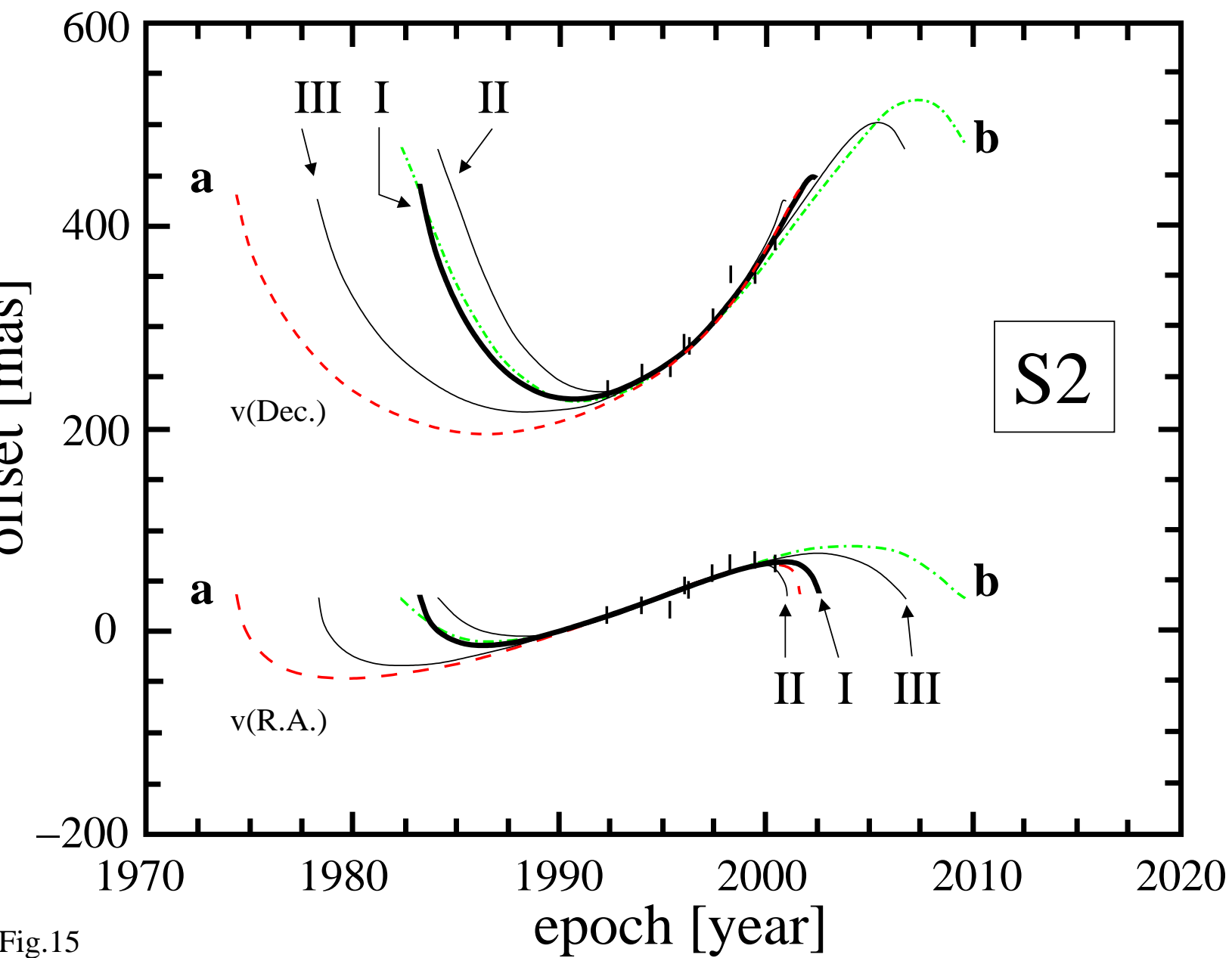


Fig.15

APPENDIX

Here we present the measured proper motion velocities and their transformation to the epochs used for the orbit calculations.

Table 7: Comparison of Proper Motion Velocities

		SHARP 1996.5		Keck 1995.4	
		v_α	v_δ	v_α	v_δ
measured:	S1	+550±90	-1440±100	+470±130	-1330±140
	S2	-330±50	-800±90	-290±110	-500±50
	S8	+490±60	-560±40	+720±80	-530±110
transformed:	S1	+531	-1480	+489	-1291
	S2	-249	-587	-371	-713
	S8	+581	-544	+629	-545
mean:	S1	+541±60	-1460±60	+480±60	-1311±60
	S2	-290±60	-694±60	-330±60	-607±60
	S8	+535±60	-552±60	+675±60	-538±60

The velocities (in km/s) were obtained for epochs 1996.5 (SHARP) and 1995.4 (Keck; Ghez et al. 1998). We used the combined 1996.5 data in Tab. 3. We combined the two data sets by transforming the velocities between epochs using the known accelerations. For the combined (mean) proper motion velocities the mean (quadratic) difference between the R.A. and Dec. velocities of those two epochs are 80 km/s (95 km/s). As expected - this error accounts for velocity differences expected over 1.2 years from the measured curvatures of the order of about 80-160 km/s/yr as a mean per coordinate. As an error for the mean velocities we used 60 km/s - obtained from the mean quadratic deviation between the individually measured and transformed velocities for each of the 3 epochs in Tab. 7 and Tab. 8.

Table 8: Proper Motion Velocities for the 1997.6 Epoch

	SHARP to epoch 97.6		Keck to epoch 97.6		mean at epoch 97.6	
	v_α	v_δ	v_α	v_δ	v_α	v_δ
S1	+606	-1576	+531	-1480	$+568 \pm 60$	-1528 ± 60
S2	-293	-879	-249	-587	-271 ± 60	-733 ± 60
S8	+364	-573	+580	-544	$+472 \pm 60$	-558 ± 60

Transforming the velocities (in km/s) observed for epochs 1996.5 (SHARP) and 1995.4 (Keck) to the time averaged Keck epoch 1997.6 (Ghez et al. 2000) using the projected accelerations in R.A. and Dec. as measured by SHARP (Tab. 1). We used the combined 1997.6 data in Tab. 3. For errors see caption to Tab. 7.